AN OPTICAL TECHNIQUE FOR MEASURING FORCE
BETWEEN A COLLOIDAL PARTICLE AND A FLAT SURFACE

By

AARON ROBERT CLAPP

A DISSERTATION PRESENTED TO THE GRADUATE SCHOOL
OF THE UNIVERSITY OF FLORIDA IN PARTIAL FULFILLMENT
OF THE REQUIREMENTS FOR THE DEGREE OF
DOCTOR OF PHILOSOPHY

UNIVERSITY OF FLORIDA

2001

This dissertation is dedicated to my parents, Robert and Deborah Clapp.

Lastly, I thank Dr. Pavel Zemánek and his colleagues at the Institute for Scientific Instruments, Academy of Sciences of the Czech Republic, for supplying various materials and offering expert opinion in the area of beam optics and optical trapping.

TABLE OF CONTENTS

LIST OF FIGURES

Abstract of Dissertation Presented to the Graduate School
of the University of Florida in Partial Fulfillment of the
Requirements for the Degree of Doctor of Philosophy

AN OPTICAL TECHNIQUE FOR MEASURING FORCE BETWEEN A COLLOIDAL
PARTICLE AND A FLAT SURFACE

By

Aaron Robert Clapp

May 2001

Chairman: Richard Dickinson
Major Department: Chemical Engineering

The behavior of colloidal particles in solution is greatly affected by the interaction

the particles have with their surroundings. This may take the form of particle–particle

interactions or the interaction of a single particle with a nearby solid wall. These

interactions are characterized by the forces that are generated as a function of the

separation distance between two surfaces. Fundamental phenomena such as particle

deposition, solution rheology, and even microbial adhesion primarily depend on the

magnitude and range of these fundamental forces as the particles move through the fluid.

Several experimental techniques can measure these small forces directly.

However, there is no existing technique for measuring forces on particles having

diameters on the order of 1 nm or less. This size range is especially important for studies

of bacterial or viral adhesion mechanisms where the nominal diameter can be much

smaller than 1 nm.

This dissertation describes a novel technique for measuring the static and dynamic forces that arise between a single colloidal particle and a flat plate. A single-beam gradient optical trap is used as a sensitive force transducer and evanescent wave light scattering is used to determine the particle position within the trap. The static force is measured by observing the equilibrium position of the particle within the trap, while the dynamic force is measured from the relaxation time of the particle fluctuations near the equilibrium position. Each force contribution is measured as a function of the particle–surface separation distance by moving the particle toward the surface in nanometer-sized increments. Absolute separation distances are determined by curve fitting the viscous force data to hydrodynamic theory in regions where the static force is negligible.

Measurements of static force agree well with classical Derjaguin–Landau–Verwey–Overbeek theory over the entire range of separation distances. Measured dynamic force agrees well with hydrodynamic theory until there is appreciable overlap of the electrical double layers at close separations. This departure may be due to a coupling of hydrodynamic and electrical phenomena that greatly enhances the viscous drag.

CHAPTER 1
INTRODUCTION

1.1 Surface Forces and DLVO Theory

Surface forces—the interactions that arise between exposed material surfaces in solution—directly influence and control the behavior of colloidal particles (with a diameter of 1 μm or less) suspended in a liquid. For example, stability of a particle dispersion, rheological behavior, and adhesion of particles from solution to other surfaces are all mediated by surface forces. A better understanding of these and other phenomena clearly necessitates a quantitative characterization of surface forces on the colloidal scale. These interactions are classified as either conservative (in the case of static forces) or non-conservative (in the case of drag forces) depending on the origin of the interaction.

In the last half-century, significant attention has been given to developing accurate predictive theories for conservative colloidal forces. Typically, these theories have been adaptations of the seminal work of Derjaguin and Landau (Russia) [1], and Verwey and Overbeek (Holland) [2], known collectively as the DLVO theory. Originally developed to predict the stability of colloidal suspensions, DLVO theory characterizes the equilibrium interaction energy between two bodies as the additive contributions of screened electrostatic and van der Waals interactions. Using various system-specific parameters (e.g., surface charge, solution ionic strength, particle size), DLVO theory predicts a potential energy profile for two interacting surfaces where a key result is the effective maximum energy required for the surfaces to contact. This maximum energy is

1

often referred to as the *energy barrier* to attachment and is directly related to the probability that the two surfaces will contact each other within a certain time interval.

DLVO theory has been used to describe the rheology of concentrated particle suspensions. Whereas more primitive models consider particles to be simple hard spheres, the inclusion of surface forces accounts for particle "softness" where the particle has a larger effective radius due to the double layer ions collected near its charge surface. Within the last thirty years, DLVO theory has also been used extensively to describe the phenomenon of bacterial adhesion [3]. Though bacterial cells are far more complicated than colloidal particles with their irregular shape, polymeric appendages, and heterogeneous structure, DLVO theory can be a useful first approximation for estimating the forces that exist between a cell and a nearby surface.

Though many predictive theories exist for colloidal forces, their success depends on the material system considered and the availability of certain parameter values which are often difficult to determine. In extreme cases, as may be the situation with suspensions of bacteria, for example, the chosen theory may be inappropriate altogether due to the invalidation of one or more critical assumptions. Often, it is desirable and more convenient, even for relatively simple systems, to measure these forces experimentally rather than rely solely on theory. In addition to the aforementioned theoretical work, there has been a similar emphasis on developing accurate experimental methods for measuring surface forces directly.

1.2 Surface Force Measurement Techniques

Three relatively recent techniques have emerged which account for most of the experimental surface force measurements performed to date. The most commonly used

of these is the surface forces apparatus (SFA) of Israelachvili and Adams [4]. The SFA

has been used in numerous studies to measure the interaction forces between mica sheets

arranged in a crossed-cylinder geometry. The surfaces may also be coated, which greatly

expands the versatility of the technique. The interaction force is measured using a

sensitive spring in combination with an interferometry technique to determine absolute

separation distances down to the angstrom level. Since the radii of the cylinders are on

the order of centimeters, the measured forces are orders of magnitude greater than those

seen in colloidal systems. Therefore, other techniques are necessary for measuring

surface forces where one of the materials has colloidal dimensions.

One of these colloidal force measurement techniques, developed by Ducker and

co-workers [5], uses atomic force microscopy (AFM) [6] to measure the interaction force

of a colloidal probe particle, attached to the end of a solid cantilever, with a flat surface.

Since the imaging principle of atomic force microscopy is inherently based on the

existence of surface forces, quantitative measurements are readily made using the force

mode of AFM. Deflections of the cantilever are accurately measured using a laser that

reflects off the back surface of the cantilever and strikes a position sensitive

photodetector. Though it is widely described as a colloidal force measurement technique,

truly colloidal spheres (with a diameter of 1 μm or less) are rarely used because of the

challenge in mounting the particle to the cantilever. AFM also has a sensitivity limit of

about 10^{-10} N which is relatively large for colloidal systems [7]. The advantage of AFM,

however, is that the particle can be reversibly attached and removed from the surface due

to the stiffness of the cantilever.

The other common experimental technique for colloidal measurements is total internal reflection microscopy (TIRM) developed by Prieve and co-workers [8]. Unique to any of the methods previously described, TIRM directly measures the potential energy of a particle near a wall rather than the force. It does this by applying Boltzmann's law, which is relates the probability of finding a particle at a given location to the potential energy at that location. In contrast to other techniques, TIRM is considered to be "non-invasive" because the particle is free to diffuse within the suspending liquid. The particle–surface separation distance is instantaneously found by measuring the scattered light emitted from the particle in an evanescent wave; we therefore call this technique *evanescent wave light scattering*. Later generations of TIRM included the use of a radiation pressure (two-dimensional) optical trap to confine the lateral movements of the particle [9]. This improved the measurements greatly by holding the scattering particle in the field of view for the duration of the experiment. Since the technique does not impose external control of the particle in the axis normal to the flat surface, the maximum measurable energy is limited by the inherent thermal energy of the particle. This means that TIRM can only effectively measure energy on the order of a few kT (where 1 kT = 4.1×10^{-21} J at 298 K). Although TIRM measures potential energy directly, the corresponding force profile is found by evaluating the negative slope of the measured energy profile. It should be noted that the radiation pressure optical trap is able to exert a constant force on the particle in addition to constraining its lateral motion. By adjusting the power of the beam, it is possible to shift the particle to regions of greater potential energy. This is especially useful if the beam exerts a pressure on the particle toward the

flat surface since this is typically in opposition to the electrostatic repulsive force. However, this method is usually not attempted in TIRM experiments.

1.3 Force Measurement Techniques for Micron-Sized Particles

Although studies of surface forces have been greatly enhanced by the techniques previously described, there still remain many colloidal systems of various size and nature that elude accurate measurement. In particular, force measurements using micron-sized particles are either difficult or impossible using existing techniques. While it would be desirable to develop a technique capable of measuring interactions for any colloidal system, the interactions between a micron-sized particle and a flat surface are particularly relevant to the study of bacterial adhesion. Many common bacteria species have nearly spherical shapes with diameters that are near (and often below) 1 μm in size. For this reason, bacteria are often considered to be simple colloidal particles even though their internal and external physical structure is far more complicated. The success of DLVO theory as a quantitative tool is usually quite poor for this reason. Most theories for bacterial adhesion are based on the original DLVO framework, but are modified to account for additional interactions; for example, steric forces are often considered as well. Of course this can lead to theories that become too complicated or phenomenological to be of much practical use, employing many more parameter values than can be readily determined or justified. For these complicated systems, direct measurements are even more important.

Until recently, TIRM has been the most suitable technique for measuring colloidal interactions. (Note, however, that the current literature contains no studies of particles with a diameter below 1 μm.) Since the measurements are non-invasive and rely only on

the ability of the particle to scatter light, particles of nearly any diameter may be used (in practical terms, this range is about 0.2 to 20 μm). Since TIRM deduces the potential energy of interaction directly, there is no preset limitation on the measurable force aside from that imposed by the resolution of particle position. However, there is a strict limitation on the maximum energy that is measurable, which is effectively set by Boltzmann's law. This inherent energy limit hinders the usefulness and practicality of TIRM measurements since the energy profile of a particle approaching a surface may far exceed these measurement limits. In addition, as the diameter of a particle diminishes, the diffusive movements increase according to the Stokes–Einstein relation. Thus, for relatively small particles (less than about 5 μm in diameter), it is difficult to record complete measurements because the particle will simply leave the active detection region before the experiment is finished.

Addressing these issues, Brown and co-workers [9, 10] adapted the original TIRM technique by adding a radiation pressure optical trap to localize the lateral position of the particle and to push the particle axially toward the flat surface into regions of higher energy. While this two-dimensional optical trap was effective at constraining transverse fluctuations, the axially directed radiation pressure force was less useful because it was a non-linear function of laser power. In order to scan the entire potential energy profile, from far away to very near the surface, the laser power would have to be discretely varied in order to advance the particle toward the surface. This is possible, but impractical because the resulting potential energy data would need to be corrected for the effect of the trap and the discrete sections pieced together to form the complete profile.

Ashkin [11] first reported development of the radiation pressure optical trap in the early 1970s at Bell Laboratories. Since that time, various trapping schemes have been implemented for a variety of research endeavors including the study of surface forces. The utility of an optical trap for the study of colloidal forces is primarily two-fold: it is essentially non-invasive to the sample and is able to impart small-scale forces to the trapped particle ranging from 10^{-12} N to 10^{-15} N. Unfortunately, the two-dimensional radiation pressure optical trap is unable to confine the particle along the beam axis and provides a constant force in the direction of propagation. However, in 1986, Ashkin and co-workers [12] introduced a single-beam gradient optical trap that was able to precisely control a particle in three-dimensions. With its simple design, one can easily build a gradient optical trap into a laboratory microscope with only minor modifications. This led to the commercialization of gradient optical trapping units, known commonly as "laser tweezers," which easily insert into many popular models of microscopes.

The most useful aspect of the gradient optical trap, in the context of force measurement, is the ability to readily quantify the three-dimensional forces acting on the particle, including those imparted in the axial direction. The intensity profile created by a tightly focused beam imposes a three-dimensional harmonic potential energy profile on the particle (the theory of which is yet to be described). That is, for any reasonably small deviation of the particle center from the region of highest intensity, there is an approximately linear restoring force that pushes the particle back to the equilibrium location. The most useful analogy to consider is that of a mass attached to three orthogonal springs, each with a characteristic spring constant and equilibrium (unstressed) position. By observing the motion of the trapped particle over time, the

equilibrium distribution of positions taken by the particle allows these effective spring constants (or alternatively, trap stiffness values) to be determined experimentally; this is known as calibrating the trap.

If the trap stiffness and focus location are known, the optical trap can be used as a force transducer in a fashion analogous to AFM force measurements with a known cantilever stiffness. In either method, the force is measured by performing a simple force balance, where the force of interaction between the particle and surface is equal and opposite to the force applied by the optical trap or cantilever at the new equilibrium position. The balance is somewhat complicated by the Brownian fluctuations of the particle, but the net forces are zero at the peak, or mode, of the equilibrium distribution of particle positions (i.e., at the minimum of total combined potential energy of the trap and the surface). The concept of using an optical trap as a force transducer is relatively simple, but it requires an accurate method of determining the particle position along the axis of interest. It is possible to monitor small movements of a particle using microscope image analysis with a resolution better than 10 nm, but this is far less effective for movements made along the microscope objective axis (into and out of the viewing plane). Image analysis is also insufficient for monitoring rapid Brownian movements.

1.4 A New Technique for Colloidal Force Measurement

To accurately measure the forces between a single micron-sized particle and a flat surface, we have developed a new technique [13] that combines a single-beam gradient optical trap as a force transducer and evanescent wave light scattering for precise measurement of particle position. In contrast to TIRM, the technique measures force directly (rather than potential energy) in a manner similar to AFM. As the trapping beam

focus is stepped toward the surface, the most probable particle position is measured at each trap position to determine the force–distance profile. The trapping force can move the particle to high-energy regions that are inaccessible through purely diffusive movements. Moreover, the time required to perform a complete force profile measurement is far less than with TIRM, even though the sampled spatial region can be much larger with the new technique. This is because a diffusing particle held by an optical trap samples the accessible energy landscape more quickly than a freely diffusing particle.

We have validated the technique by measuring conservative (static) forces between colloidal silica spheres (~1 μm in diameter) and a flat glass plate in aqueous solutions of varying ionic strength. These forces usually include screened electrostatic (double layer) and van der Waals interactions, or those typically described by DLVO theory. In addition, we have extended the technique to simultaneously measure the non-conservative forces that arise as a particle nears a flat surface. Non-conservative (dynamic) forces depend on the motion of the particle as well as its position from the surface. Usually, this is simply the hydrodynamic drag force as the particle moves through the fluid. We have compared our experimental force results with DLVO theory predictions (for static forces) and a modified version of Stokes' law (for dynamic forces) in order to assess the accuracy of the data and validate the technique.

1.5 Outline of the Dissertation

Chapter 2 discusses necessary theoretical background required for the understanding of essential concepts of electrical double layer forces, van der Waals forces, colloidal hydrodynamics, evanescent wave light scattering, and optical trapping.

Chapter 3 describes our new technique with details of the experimental procedure and data analysis. Chapter 4 gives experimental results of the initial static force measurements and a discussion of persistent interference effects that significantly altered the results. Chapter 5 describes a modified methodology for measuring static and dynamic forces more accurately. The results of these experiments were shown to validate the technique's accuracy. Chapter 6 describes methods for simulating and modeling the experiments in order to make predictions about the experimental data. Finally, Chapter 7 summarizes some key observations from our experiments and offers some suggestions for future work.

CHAPTER 2
THEORY

2.1 Electrical Double Layer

Electrostatic forces arise between materials immersed in solution when there is a net charge on the surfaces. The interceding medium between the exposed surfaces generally contains dissolved ions that serve to screen the purely coulombic interactions. Before we can predict the forces that arise between two surfaces in solution, we must first consider how the electrostatic potential varies with distance from the surface. This requires an examination of the charges that exist on the surface and how ions in solution are distributed.

Exposed surfaces in solution can acquire a net charge through a variety of mechanisms. When a solid is brought into contact with a polar medium like water, charge may be acquired through ionization of surface groups, isomorphic substitution in the solid lattice structure, or adsorption of *potential determining ions*. The resulting surface charge determines the distribution of ions in the polar medium attracting ions of opposite charge (*counterions*) toward the surface, and repelling ions of similar charge (*co-ions*) away from the surface. The redistribution of ions near a surface creates an *electrical double layer*, a conceptual division of the charged region (including the surface and nearby ions) into distinct bulk phases that carry equal and opposite charge. Typically, though, the term "double layer" simply describes the diffuse ion atmosphere near the surface. We will adopt this latter usage and use it throughout.

2.1.1 Poisson–Boltzmann Equation

The variation of potential from a surface is a well-known problem in classical electrostatics. It is described by the Poisson equation:

$$\nabla^2 \boldsymbol{y} = -\frac{\boldsymbol{r}^*}{\boldsymbol{e}}, \tag{2.1}$$

where ∇^2 is the Laplacian operator, $\boldsymbol{y}$ is the electrostatic potential, $\boldsymbol{r}^*$ is the charge density, and $\boldsymbol{e}$ is the dielectric constant of the liquid. In order to solve equation (2.1) for potential, there must be an expression for the charge density as a function of the potential. Using the thermodynamic result known as *Boltzmann's relation* to describe the probability of finding an ion at a particular distance from a flat surface where the potential is $\boldsymbol{y}$, we arrive at

$$\boldsymbol{r}^* = \sum_i z_i\, e\, n_{i\infty} \exp\left(-\frac{z_i e \boldsymbol{y}}{kT}\right), \tag{2.2}$$

where z_i is the valance number of ion type i, e is the proton charge, $n_{i\infty}$ is the number of ions far from the surface, k is Boltzmann's constant, and T is the absolute temperature. The combined form of equations (2.1) and (2.2) is known as the *Poisson–Boltzmann* (PB) *equation*:

$$\frac{d^2 \boldsymbol{y}}{dx^2} = -\frac{e}{\boldsymbol{e}} \sum_i z_i\, n_{i\infty} \exp\left(-\frac{z_i e \boldsymbol{y}}{kT}\right), \tag{2.3}$$

where x is the spatial dimension in the above one-dimensional form. (Note that future sections will have z as the distance variable, but x is chosen here to avoid confusion with the valence number, z_i.) While the PB equation fully describes the variation of potential from the surface, it is usually difficult to solve since the Boltzmann factor introduces an exponential term rendering the equation non-linear; in fact, no generalized analytical solution exists. There are, however, other solutions for the potential as a function of distance from the surface for certain limiting cases discussed below.

2.1.2 Debye–Hückel Approximation

It is possible to solve the non-linear Poisson–Boltzmann (NLPB) equation numerically, but this usually is not attempted since it is often cumbersome and would have to be solved each time the conditions are varied. If we take a series expansion of equation (2.2) and keep only the first term, we can solve a linearized form of the PB equation known as the *Debye–Hückel approximation*:

$$\frac{d^2\boldsymbol{y}}{dx^2} = \left[\frac{e^2}{\epsilon kT} \sum_i z_i^2 \, n_{i\infty}\right]\boldsymbol{y} = \boldsymbol{k}^2\boldsymbol{y}, \tag{2.4}$$

where $\boldsymbol{k}$ is a constant parameter, the inverse of which is known as the *Debye length* or the *double layer thickness*, $\boldsymbol{k}^{-1}$ [15]. Note that, at constant temperature, the Debye length is purely a function of the electrolyte content of the solution. The solution to the linearized PB equation is simply

$$\boldsymbol{y} = \boldsymbol{y}_0 \exp(-\boldsymbol{k}x). \tag{2.5}$$

The Debye–Hückel approximation is accurate for surface potentials below kT/e (~25 mV at 298 K). In practical terms, it remains reasonably accurate for potentials up to about 60 mV. The solution given by equation (2.5) also assumes a fixed surface potential, y_0, at one boundary, and $y \to 0$ as $x \to \infty$ at the other. In this model, the relationship between surface charge density, $s\,^*$, and surface potential, y_0, is assumed linear, which is analogous to a parallel plate capacitor with a separation distance of k^{-1}.

2.1.3 Gouy–Chapman Theory

The usefulness of the Debye–Hückel approximation is hampered by many simplifying assumptions, so we turn to a more generalized solution of the PB equation, known as *Gouy–Chapman theory*, to describe the potential profile for any value of the surface potential. The derivation of the final Gouy–Chapman result is somewhat lengthy so it is not shown here, but the final expression is important to note. Returning to equation (2.3), we allow the surface potential to take any value and integrate the equation assuming the solution electrolyte is symmetric ($z : z$) and such that the two boundary conditions of the equation are imposed at infinite distance from the surface where $y(x)$ and $y'(x)$ both approach zero. The final result is

$$\tanh\left(\frac{zey}{4kT}\right) = \tanh\left(\frac{zey_0}{4kT}\right)\exp(-kx), \tag{2.6}$$

which can be simplified to

$$\Upsilon = \Upsilon_0 \exp(-kx). \tag{2.7}$$

Note that the Gouy–Chapman expression is an analytical solution, but it requires a symmetric electrolyte. Similar to the Debye–Hückel result in equation (2.5), the above equation shows an exponential variation with distance, however it is now a transcendental function of the potential, Υ , that is exponentially varying rather than the potential itself. As we might expect, as the surface potential tends below 25 mV, equation (2.7) approaches equation (2.5) demonstrating that the Debye–Hückel approximation is a subset of the more general Gouy–Chapman theory.

2.1.4 Stern Model

To this point, we have only considered ions in solution that are "indifferent" to the surface. In other words, the models have assumed that the ions are not able to attach to the surface. In addition, we have not accounted for the size of the ions, which becomes important for larger potentials where ions will tend to adsorb and saturate binding sites on the surface. In the model proposed by O. Stern [16], the double layer extending into solution is divided by an imaginary boundary known as the *Stern surface*. The Stern surface, also called the *inner Helmholtz plane* (IHP), runs through the adsorbed ions at distance ***d*** from the solid surface. Just beyond the IHP is the *outer Helmholtz plane* (OHP) which defines the *shear surface* beyond which the ions are freely diffusing (as in the Gouy–Chapman model). Figure 2-1 illustrates the Stern model of the electrical double layer.
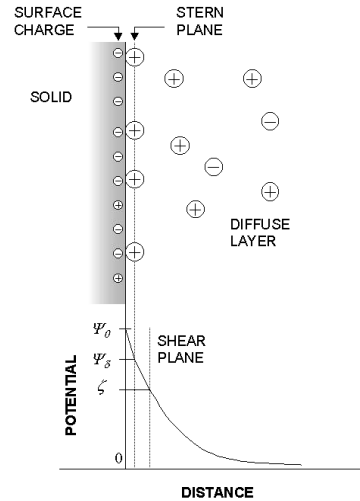
Figure 2-1. Schematic of the Stern model for the electrical double layer.

Within the Stern layer, the potential is simply modeled as a parallel plate capacitor with a linear potential drop from the solid surface out to distance d. Beyond the Stern surface, the potential follows a model for the diffuse double layer like the Gouy–Chapman result in equation (2.7). In practice, the Stern model is almost never used because several parameters remain unknown. However, the model does suggest that adsorption is important to the formation of the double layer, and that the actual value of the surface potential may be markedly different from values measured by experimental methods. For this reason, it is customary practice for the surface potential to be characterized by the potential at the shear plane rather than at the solid surface. The potential at the shear plane is called the *zeta potential* and may be found using common electrokinetic experimental techniques like electrophoresis and streaming potential measurements.

2.1.5 Calculating Force and Energy

Now that we have developed expressions for the potential as a function of distance from the surface, we can find equations for the interaction force and energy between two charged surfaces in solution when their double layers overlap. The total force on an infinitesimal volume element, dV, at some location between the surfaces is the addition of the osmotic pressure (along the x-direction) and the *Maxwell pressure* (electrical stress) contributions. At equilibrium, the total force equals zero and we can integrate an expression to find the force *per unit area* between the surfaces as a function of the distance between the flat surfaces, h. The result is

$$F_R(h) \approx 64kTn_\infty \tanh^2\left(\frac{ze\mathbf{y}_0}{4kT}\right)\exp(-\mathbf{k}h), \tag{2.8}$$

which is an approximate expression that assumes slightly overlapping double layers and identical surface potentials. This assumption, called the *superposition approximation*, allows us to estimate the potential distribution between the surfaces using the Debye–Hückel result for single surfaces rather than requiring us to resolve for the potential between two surfaces explicitly. Since force and energy are related by $F = -\nabla \mathbf{f}$, we can integrate equation (2.8) to find the interaction energy per unit area:

$$\hat{\mathbf{f}}_R(h) \approx 64kTn_\infty \mathbf{k}^{-1} \tanh^2\left(\frac{ze\mathbf{y}_0}{4kT}\right)\exp(-\mathbf{k}h). \tag{2.9}$$

Unfortunately, equations (2.8) and (2.9) are not particularly useful for colloidal interactions where at least one surface has a small radius of curvature. In most cases, we

are interested in the interactions between two spheres in solution, or a sphere and a flat plate, where the surfaces may have differing surface potentials. To account for this, the usual case is to solve some form of the PB equation (typically a power series expansion of the NLPB equation) in the space between the surfaces where the boundary conditions are $\boldsymbol{y} = \boldsymbol{y}_{0_1}$ at $x = 0$ and $\boldsymbol{y} = \boldsymbol{y}_{0_2}$ at $x = h$. The energy per unit area is calculated directly and expressed in integral form by a *charging process*, described by Verwey and Overbeek [2], where each surface potential remains fixed. To find the interaction energy between two spheres, we use *Derjaguin's approximation* [17], which integrates the interaction energy produced by opposing infinitesimal rings, each of which are considered to be flat surfaces:

$$\boldsymbol{f}_R(h) = \frac{2\boldsymbol{p} a_1 a_2}{a_1 + a_2} \int_h^\infty \hat{\boldsymbol{f}}_R(h')dh', \tag{2.10}$$

where a_1 and a_2 are the radii of the spheres, and $\hat{\boldsymbol{f}}_R$ is the interaction energy per unit area. Note that we can consider a sphere interacting with a flat plate by allowing one radius to become infinite. Derjaguin's approximation assumes the radii to be much larger than both the double layer thickness, $\boldsymbol{k}^{-1}$, and the separation distance, h.

Hogg, Healy, and Fuerstenau [18], and later Wiese and Healy [19], derived expressions for the interaction potential between two dissimilar spheres using the Debye–Hückel approximation:

$$\boldsymbol{f}_R(h) = \frac{\boldsymbol{e} a_1 a_2 \left(\boldsymbol{y}_{0_1}^2 + \boldsymbol{y}_{0_2}^2\right)}{4(a_1 + a_2)} \left[\frac{2\boldsymbol{y}_{0_1}\boldsymbol{y}_{0_2}}{\left(\boldsymbol{y}_{0_1}^2 + \boldsymbol{y}_{0_2}^2\right)} \ln\left(\frac{1 + e^{-kh}}{1 - e^{-kh}}\right) \pm \ln\left(1 - e^{-2kh}\right) \right], \tag{2.11}$$

where the "±" symbol becomes positive for constant surface potential or negative for constant surface charge. Constant surface potential assumes that surface charge is acquired through the adsorption of potential-determining ions, whereas constant surface charge assumes that charge arises due to the ionization of surface groups. For typical colloidal materials, a constant surface charge assumption is more suitable although many more sophisticated models for double layer forces are based on a constant potential assumption; the reason for this is not clear. The two cases given in equation (2.11) are limiting cases of intermediate *charge regulation* models that may be more complicated.

For most practical situations, equation (2.11) is sufficient to estimate the interaction energy between two surfaces. There are, of course, many other equations for double layer interactions that are more recent and, unfortunately, far more complicated than those presented here. Some interesting examples are given by Ohshima et al. [20], Grant and Saville [21], and Sader et al. [22]. Usually, these equations are valid over a broader range of conditions (e.g., surface potential, separation distance) and consider other complicating factors.

2.2 van der Waals Forces

The tendency of the electrons in molecules to have an uneven spatial charge distribution leads to the formation of dipoles. The ability of these molecular dipoles to interact based on atomic polarizability and the generation of electric fields is a phenomenon classified as *van der Waals* interactions. A defining characteristic of van der Waals forces is that they are ubiquitous; electrostatic forces, for example, require a net charge on each surface. In addition, van der Waals forces are nearly always attractive

whereas electrostatic forces may be either attractive or repulsive depending on the surface chemistry.

2.2.1 Molecular Dipole Interactions

Molecular-level van der Waals forces determine interactions between macroscopic bodies. One type of molecular interaction occurs between two permanent dipoles. The dipoles are assumed to be isolated in a vacuum with sufficient thermal energy to ensure free rotation. Using a Boltzmann average over all possible configurations and giving more weight to favorable energies, the free energy of interaction between two freely rotating dipoles is

$$f_K(r) = -\frac{2m_1^2 m_2^2}{3(4\pi\varepsilon_0)^2 kTr^6} = -\frac{C_K}{r^6}, \tag{2.12}$$

where m_i is the dipole moment of molecule i, r is the intermolecular distance, and C_K is a characteristic constant. The above expression was first derived by W. H. Keesom [23] and is known as the *Keesom equation*.

A second type of interaction occurs between an induced dipole and a permanent dipole. P. Debye [24] derived the following result:

$$f_D(r) = -\frac{m_1^2 a_2 + m_2^2 a_1}{(4\pi\varepsilon_0)^2 r^6} = -\frac{C_D}{r^6}, \tag{2.13}$$

where a_i is the atomic polarizability of molecule i, and C_D is a characteristic constant. This expression is known as the *Debye equation*.

The last type of interaction occurs between two induced dipoles. London first

solved the quantum mechanical model of two dissimilar hydrogen-like atoms to yield

$$f_L(r) = -\frac{3a_1 a_2 h n_1 n_2}{2(4\pi e_0)^2 (n_1 + n_2)r^6} = -\frac{C_L}{r^6},$$ (2.14)

where h is Planck's constant, n_i is the oscillatory frequency of molecule i, and C_L is a

characteristic constant. This expression is known as the *London equation* for dissimilar

molecules. This type of interaction is sometimes referred to as the *dispersion interaction*

because its role in a phenomenon related to the scattering of light (not the dispersion of a

colloidal solution).

Upon inspection of the preceding three equations, we notice that they all share the

same power law dependence, r^{-6}, and can be combined to form the overall van der

Waals equation for intermolecular free energy:

$$f_{vdW}(r) = -\frac{(C_K + C_D + C_L)}{r^6} = -\frac{C_{vdW}}{r^6}.$$ (2.15)

Regardless of the material, there will always be a contribution from the London

(dispersion) interaction since it does not depend on the existence of a permanent dipole

(i.e., a non-zero value of m). In general, the London interactions dominate the other two.

However, water molecules present a notable exception to this tendency where the

Keesom interactions account for most of the overall van der Waals attraction.

2.2.2 Macroscopic Interactions

With expressions for the molecular interactions between dipoles, we can integrate all pairwise interactions occurring between the molecules in two macroscopic bodies. This is the approach used by H. C. Hamaker [25] for solving the macroscopic interaction energy between objects of various geometries. For the case of two interacting spheres, the van der Waals interaction energy is

$$f_{vdW}(h) = -\frac{Aa_1a_2}{6h(a_1 + a_2)},$$ (2.16)

where A is the Hamaker constant, h is the minimum separation distance, a_1 and a_2 are the radii of the spheres. The Hamaker constant characterizes the magnitude of the attraction and varies by material. As with the double layer energy equation for two spheres, a sphere–plate geometry is considered by allowing one radius to become infinite.

The value of the Hamaker constant depends on the types of materials considered, including the interceding medium between the two bodies. In general, the Hamaker constant A_{ijk} represents the interaction between materials i and k across medium j. If we have Hamaker constant values for all three materials interacting with themselves in vacuum (A_{11}, A_{22}, and A_{33}), we can estimate the effective Hamaker constant for the overall system:

$$A_{132} = \left(A_{22}^{1/2} - A_{11}^{1/2}\right)\left(A_{33}^{1/2} - A_{11}^{1/2}\right),$$ (2.17)

which is based on a chemical reaction analogy, the details of which are omitted.

Equation (2.16) is commonly used to describe the van der Waals attraction between macroscopic bodies, but it is not particularly accurate for separation distances above about 10 nm   this is due to a *retardation* of the London interactions [7]. The interaction between induced dipoles is significantly affected by the distance between the materials because of the finite propagation speed of the electric field and the temporal nature of the induced dipole. Even though the propagation speed is equal to the speed of light, *c*, the induced dipoles themselves are rapidly fluctuating. This introduces a lag effect that reduces the interaction of the temporary dipoles as the distance between them increases. To account for this, a time-dependent quantum analysis is used for the London interactions, which yields a power law of r^{-7} beyond a characteristic distance.

The most rigorous method of calculating the van der Waals attraction between macroscopic bodies is known generally as *Lifshitz theory* [26]. Lifshitz theory uses bulk dielectric properties to evaluate van der Waals energy rather than the sum of all molecular pairwise interactions proposed by Hamaker. This approach has built into it retardation effects and the effect of the interceding medium we mentioned earlier. As a result, the calculated Hamaker constant is a misnomer: it varies with increasing separation distance and specific dielectric properties.

While it is by far the most accurate means of calculating van der Waals interactions, Lifshitz theory is usually very difficult to implement. The calculations are tedious and rely on dielectric data that is often unavailable. This has led to the development of approximate expressions that reasonably accurate for most practical applications. Gregory [27] presents several of these approximate expressions with a discussion of their applicability.

2.3 DLVO Theory

In the 1940s, two groups of scientists independently developed quantitative theories for the kinetic stability of colloids. They included Russian physicists B. V. Derjaguin and L. D. Landau [1], and Dutch chemists E. J. W. Verwey and J. Th. G. Overbeek [2]. Hence, theories that describe the interaction energy that arises between surfaces are collectively known as *DLVO theory*. DLVO theory assumes that there are two primary contributions to the interaction energy, the electrostatic (double layer) and van der Waals interactions, and that these contributions are additive:

$$\boldsymbol{f}_{DLVO} = \boldsymbol{f}_R + \boldsymbol{f}_{vdW}, \qquad\qquad (2.18)$$

where $\boldsymbol{f}_R$ and $\boldsymbol{f}_{vdW}$ are appropriate expressions of energy for the geometry and materials of interest. A typical plot of the DLVO interaction energy is shown in Figure 2-2.
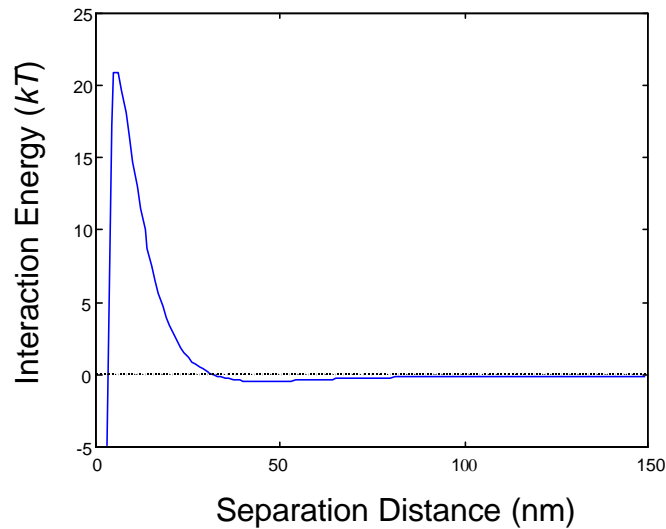
Figure 2-2. DLVO interaction energy between a sphere and a flat plate.

The precise shape of the potential energy curve depends on the parameter values chosen. The plot in Figure 2-2 considers a silica sphere interacting with a flat silica surface in water where the following values are used: $k^{-1} = 7$ nm, $y_{0_1} = y_{0_2} = -10$ mV, $A_{131} = 8.3 \times 10^{-21}$ J (silica–water–silica), and $a = 0.5$ *m*m.

The parameter values should represent actual experimental conditions, so it is useful to understand how these values can vary. The most readily adjustable parameter is the Debye length, which was noted previously to be a function of ionic strength:

$$k^{-1}[m] = \frac{3.04 \times 10^{-10}}{|z| M^{1/2}} \qquad (2.19)$$

where k^{-1} is in meters, M is the molarity of the solution in moles/dm^3, and z is the valence number of a symmetric electrolyte [14]. By simply changing the concentration of salt in the bulk solution, we can greatly alter the interaction energy between suspended materials. Consequently, this is a convenient way of controlling the behavior of a colloidal suspension.

The surface potential can be adjusted by adding potential determining ions, specifically adsorbing ions, or by changing the pH of the solution. If the charge on the surface is due to ionization, the latter method is a useful means of controlling the double layer interactions. A change in pH can easily render a stable suspension unstable (or vice versa) by adjusting the surface potentials. An especially difficult parameter to adjust is the Hamaker constant since it depends on the dielectric properties of the materials rather than the solution conditions. While the addition of salt to the solution does little to affect

the Hamaker constant, it does affect the screening of van der Waals forces whereby the salt ions tend to reduce the attractive interactions. The final parameter to mention is the radius. Expressions for double layer and van der Waals interactions show that the overall magnitude of the DLVO energy is proportional to the radius of curvature.

It is useful to point out several key features of the DLVO curve shown in Figure 2-2. At large separations, there is no interaction between the surfaces and the energy tends to zero. As the negatively charged surfaces approach each other, however, there is typically an appreciable *energy barrier* (maximum) to overcome in order for attachment to occur. The steep descent of the energy very near the surface forms the *primary energy minimum*. Higher values for the surface potential and Debye length tend to increase the repulsive energy and the net energy barrier; this acts to stabilize a colloidal system, encouraging particles to remain dispersed in solution. A large value of the Hamaker constant will lower the repulsive energy and net energy barrier, but its value is usually fixed for a given system, unlike the other parameters mentioned.

For a specialized combination of parameter values, the potential energy curve can show a *secondary energy minimum*. Unlike the primary minimum which is essentially infinitely deep, the secondary minimum usually has a shallow depth on the order of the thermal energy. This means that the surfaces may loosely aggregate around the location of the minimum, but the lack of depth of the minimum will allow them to be easily separated again. In the case of a sphere–plate interaction, a colloidal particle may diffuse into the secondary minimum, spend some time there, and then naturally diffuse away. The probability that a particle can escape an energy well with a particular depth in a finite amount of time is determined by the height of the energy barrier over which the particle must move to escape. For energy barriers on the order of a few kT, the probability is

reasonably high for escape. However, even if the barrier a modest value of 10 kT, the

escape probability for the particle is extremely small.

2.4 Hydrodynamics of a Diffusing Sphere

Colloidal particles are small enough such that the persistent collisions from the

surrounding fluid molecules will induce a net random movement known as *Brownian*

motion. The magnitude of motion can be modeled as a series of independent random

walks, where each step in the walk is described by classical mechanics. If a particle

acquires an initial velocity, v_0, at the start of a random walk, the subsequent motion is

described by

$$m\frac{d^2 x}{dt^2} = -\boldsymbol{d}\frac{dx}{dt} \tag{2.20}$$

where m is the mass of the particle, x is the position of the particle from the origin, and $\boldsymbol{d}$

is the drag coefficient. This equation shows a balance between the inertial force and the

viscous drag force. From equation (2.20) we see that the velocity of the particle decays

exponentially with time:

$$v(t) = v_0 \exp(- t/\boldsymbol{t}_m) \tag{2.21}$$

where $\boldsymbol{t}_m$ is the characteristic relaxation time of the particle's momentum ($\boldsymbol{t}_m \equiv m/\boldsymbol{d}$).

Although the movement is purely random, the average movement away from the initial

position is zero, and the mean-square displacement of the particle in any one direction is

simply

$$\left\langle x^2 \right\rangle = 2Dt \qquad (2.22)$$

where D is the diffusion coefficient of the particle. The diffusion coefficient and drag coefficient are related by the Stokes–Einstein relation:

$$D = \frac{kT}{d}. \qquad (2.23)$$

Many colloidal particles can be treated as perfect spheres, which allows for relatively straightforward hydrodynamic modeling. Stokes' law gives the drag force on a rigid sphere moving in a quiescent fluid at low Reynolds numbers ($Re < 1$):

$$F_{drag} = -dv, \qquad (2.24)$$

and the drag coefficient is defined as

$$d = 6\pi h a \qquad (2.25)$$

where h is the fluid viscosity and a is the radius of the sphere. Stokes' law is only rigorously valid for an uncharged particle moving within an unbounded medium. In terms of experimental force measurements, however, the particle will be diffusing very near a solid wall. This situation requires a correction to Stokes' law:

$$F_{drag} = 6\boldsymbol{ph}a\boldsymbol{l}v \qquad (2.26)$$

where $\boldsymbol{l}$ is a dimensionless correction factor whose expression depends on the direction of the movement and the type of boundary. For our purposes, we are concerned with the sphere's motion with respect to a solid flat surface. There are two expressions to consider in this geometry: corrections for the normal and parallel translations of the sphere near the flat wall. Because force profiles are measured as a function of normal separation distance, z, we restrict our attention to the normal correction factor:

$$\boldsymbol{l}(z) = \frac{4}{3}\sinh \boldsymbol{a}\sum_{n=1}^{\infty}\frac{n(n+1)}{(2n-1)(2n+3)}\times\left[\frac{2\sinh(2n+1)\boldsymbol{a}+(2n+1)\sinh 2\boldsymbol{a}}{4\sinh^2\left(n+\frac{1}{2}\right)\boldsymbol{a}-(2n+1)^2\sinh^2 \boldsymbol{a}}-1\right] \qquad (2.27)$$

where

$$\boldsymbol{a} = \cosh^{-1}\left(\frac{z+a}{a}\right). \qquad (2.28)$$

The correction factor is highly sensitive to separation distance as shown by Figure 2-3.
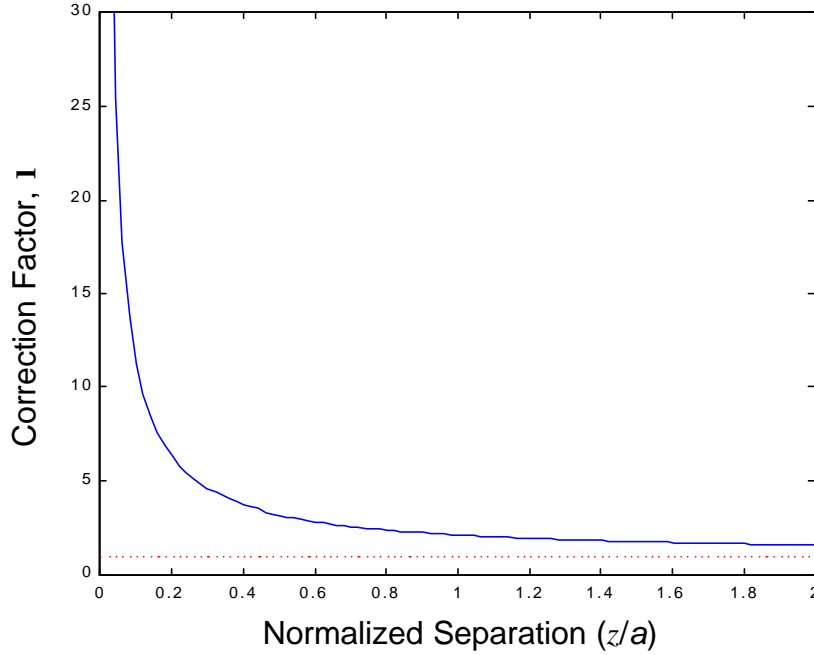
Figure 2-3. Drag force correction factor for a sphere moving normal to a solid surface.

At large separations, the correction factor is unity and Stokes' law holds (dotted line).

However, as the separation distance diminishes to zero (particle–surface contact), the

correction factor approaches infinity. Even for separations on the order of several

particle diameters ($z/a \sim 20$), the correction factor is significant and the effect of the

solid wall cannot be neglected [33].

The double layer also affects the drag force on a diffusing colloidal particle. The

ions contained within the shear plane move with the particle, effectively increasing its

radius. Additionally, the diffuse ions beyond the shear plane have a deformed

distribution with movement of the particle, thereby creating a dipole. Several authors

have derived correction factors to account for the effect of the double layer on the drag

force. Ohshima et al. gave a recent expression for this correction:

$$\boldsymbol{I} = 1 + \bar{b}\,\Phi_s^2\,f(\boldsymbol{ka}) \tag{2.29}$$

where $\bar{b}$ is a value related to the average ion size, Φ_s is the reduced zeta potential ($= ze\boldsymbol{V}/kT$), and f is a function of $\boldsymbol{ka}$. The function f is a maximum at $\boldsymbol{ka} = 1$ and tends to zero as $\boldsymbol{ka}$ approaches either zero or infinity. Typical colloidal systems used during force measurements have a large value of $\boldsymbol{ka}$ (>10) such that this correction can be safely neglected. However, if the sphere approaches a flat surface such that the opposing double layers begin to overlap, there may be a significant effect of this interaction on the drag force. Presently, little is known about this effect from either a theoretical or experimental perspective.

2.5 Evanescent Wave Light Scattering

Experimental techniques that measure force–distance profiles generally require a means for measuring position accurately. In AFM, a laser beam is reflected off the back of the cantilever to monitor minute fluctuations of the cantilever over time. Using a sensitive quadrapole (position sensitive) photodiode, fluctuations on the order of 1 nm can be measured. SFA uses an even more accurate position detector based on interferometry with resolution on the order of 1 Å. The task of measuring the trajectory a freely diffusing micron-sized sphere in solution is a bit more complicated, however—a useful solution to this problem, as we will see, is one of the novel aspects of TIRM.

Total internal reflection of light at the interface between two transparent media of differing refractive index leads to the formation of an *evanescent wave* in the optically rarer medium [28]. (Note that experiments often use a flat glass plate in contact with

water, so we will consider this special case henceforth.) The intensity of the resulting

evanescent wave decays exponentially with distance from the interface. Solving the

generalized Mie scattering problem, Chew et al. [29] showed that a spherical particle

with a refractive index dissimilar to that of the suspending medium scatters light with an

intensity that diminishes exponentially with increasing separation:

$$I(z) = I_0 \exp(-bz), \tag{2.30}$$

where z is the particle–surface separation distance, and I_0 is the scattered intensity at

zero separation (particle–surface contact). The characteristic decay constant is

$$b = \frac{4p}{l_0} [n_1^2 \sin^2 q_i - n_2^2]^{1/2}, \tag{2.31}$$

where l_0 is the wavelength of reflected light a in vacuum, n_1 and n_2 are the refractive

indices of the flat surface and the surrounding medium, respectively, and q_i is the

incident angle. Notice that adjusting the incident angle of the light (typically a laser

beam) directly affects the value of b. For physical significance, we commonly refer to

the inverse of the decay constant, b^{-1}, as the *penetration depth*.

Rearranging equation (2.30) to find separation distance yields

$$z = -b^{-1} \ln I + b^{-1} \ln I_0. \tag{2.32}$$

This result shows that we can directly relate the measured intensity to the separation distance of the particle from the surface. In general, the value of I_0 is difficult to determine experimentally since the particle must overcome the energy barrier and contact the surface irreversibly. However, in the absence of an intensity measurement at contact, equation (2.32) can be used to find *relative* separation distances from an arbitrary reference position. (Later, we will describe methods for determining *absolute* separation distances.)

The above method of calculating position from scattered intensity measurements is called *evanescent wave light scattering* (EWLS). Depending on the measurement equipment used (i.e., photodetector, data acquisition system), the technique is able to resolve distances on the order of 1 nm. The first practical use of EWLS for position measurement was seen with the development of TIRM. TIRM uses Boltzmann's law where the potential energy profile between a sphere and a plate is directly determined by measuring the equilibrium distribution of particle positions from the surface:

$$\mathbf{f}(z) = -kT \ln(\ p(z)) + C \qquad (2.33)$$

where $p(z)$ is the *probability density* of locating the particle between z and $z + dz$ from the surface, and C is a constant required to normalize the distribution. EWLS is used to experimentally determine the equilibrium probability density $p(z)$ by measuring the movement of a particle for a time period much larger than the relaxation time of particle fluctuations. By converting time-series intensity data to distances using equation (2.32), and generating a histogram of measured positions, we can find $p(z)$. Given the equilibrium distribution, the interaction energy is easily calculated using equation (2.33).

2.6 Optical Trapping

The ability of light to impart forces on macroscopic bodies is well-known. Centuries ago, Johannes Kepler first postulated that the sun exerted a radiation pressure on orbiting comets, leading to the formation of their distinctive dust tails. Classical physics can help our understanding of this behavior. Since photons possess momentum as they propagate, Newton's second law suggests that a change in the momentum of a photon requires a force. The phenomena of refraction, absorption, and reflection of electromagnetic radiation therefore all confer a force to the material with which they are interacting.

In 1970, Ashkin [11] found that a laser beam of modest power could be used to manipulate particles of colloidal dimensions, especially if the particles were neutrally buoyant (or nearly so) in a suspending solution. His early work produced a radiation pressure optical trap that could confine a particle laterally in the axis of the beam and simultaneously accelerate the particle along the direction of beam propagation. This trap is considered to be two-dimensional because it can only hold the particle in the radial direction along the beam axis. If desired, a particle could be stabilized by using gravity to oppose a constant upward radiation pressure, or by using two counter-propagating traps to create a stable trapping location between them.

By 1986, Ashkin and co-workers [12] had developed a *single-beam gradient trap* that could confine a particle in three-dimensions. In this version of the optical trap, a high numerical aperture lens is used to focus the beam down to a diffraction-limited spot. The gradient force exceeds the scattering force along the beam axis to confine the particle to a position near the focal point. Since its introduction, the single-beam gradient trap

has been used extensively (more so that its radiation pressure counterpart) in a variety of applications including force measurement.

2.6.1 Optical Trapping Models

The scattering of photons causes a radiation pressure force that tends to push a particle in one direction. In a single-beam gradient trap, a significant gradient force is generated to overcome tendency to destabilize and accelerate the particle along the beam axis. The scattering and gradient force components are often defined as

$$F_{scat} = \frac{Q_{scat}n_2 P}{c},$$
(2.34)

$$F_{grad} = \frac{Q_{grad}n_2 P}{c},$$
(2.35)

where Q is an efficiency term for the momentum transfer, n_2 is the refractive index of the surrounding medium, P is the laser power, and c is the speed of light in a vacuum [30].

The gradient force arises from the interaction of dipoles within a dielectric medium with a strong electric field. A tightly focused beam of light produces strong electric field gradients in three-dimensions near the focal point. The gradient force is proportional to the intensity gradient acting in the direction of the gradient:

$$F_{grad}(z,r) = \frac{2\pi n_2 a^3}{c}\left(\frac{m^2 - 1}{m^2 + 2}\right)\nabla I(z,r),$$
(2.36)

where *a* is the sphere radius, *m* is the ratio of the sphere's refractive index to that of the surrounding medium ($= n_1/n_2$), and *I* is the intensity distribution in cylindrical coordinates. The gradient force tends confine a particle near the region of maximum intensity (in the usual case where $m > 1$) while the scattering force tends to disrupt stable trapping. This competition between forces usually results in an equilibrium trapping location a small distance away from the focal point along the beam axis.

Most theoretical treatments of optical traps consider two limiting size regimes. The large particle limit, known as the *ray optics* (RO) or *Mie regime*, assumes the particle to be much larger than the wavelength of light ($a \gg \mathit{l}$). In this model, the focused beam is composed of individual light rays that are focused to a point, ignoring diffraction effects. The rays refract and reflect at the surface of the particle where the change in momentum of the ray, as it interacts with the particle, determines the applied force. The overall force on the particle is simply a vector sum of the forces applied by all the rays present in the convergent beam. If we have values for the Fresnel reflection coefficient (the fraction of the ray reflected at the interface), and the refractive indices of both media, we can determine the trapping efficiency parameter *Q* by simply applying Snell's law at the boundaries. We can determine the trapping force, which is independent of particle size, as a function of particle position within the trap by solving the RO model for various locations of the particle.

In many cases the RO model is unsatisfactory, especially if and the beam is tightly focused. In this case we cannot ignore diffraction effects, and usually we must also account for the complex electromagnetic (EM) fields that are created near the focal point. This leads us to the other limiting case, known as the *Rayleigh regime*, which assumes that the particle radius is much smaller than the wavelength of light ($a \ll \mathit{l}$).

Using an EM model, we attempt to approximate the electric and magnetic fields formed

by the focused laser beam and solve for the interaction force by integrating the *Maxwell*

stress tensor over the surface of the particle. In fact, regardless of the particle size, the

rigorous method of solving for the force is to use the *generalized Lorentz-Mie scattering*

theory (GLMT) based on an EM perspective. The Rayleigh limit is particularly useful

because the particle is considered to be a simple dipole, which simplifies the calculations

dramatically and yields accurate theoretical forces. In this limit, the force scales with a^3,

or the volume of the particle. Difficulties appear in the intermediate size regime where

$a \sim 1$. Here, interference effects become important, and even higher-order

approximations of the fields do not give satisfactory results. Unfortunately, many

experiments are performed in this intermediate regime where neither RO nor EM theory

works particularly well.

Recently, Tlusty et al. [31] developed a model that extended the dipole

approximation to a particle of any size. In this model, the interactions between the

particle and focused beam are considered to occur in a localized region equal to the *spot*

size, $2w_0$, of the focused beam, where w_0 is the beam waist radius. Within this localized

region, the phase of the fields does not vary appreciably, and thus the contributions to the

interactions are far less than those due to variations in amplitude. Their result has been

used widely as a means of predicting trapping forces for any size of particle.

2.6.2 Trap Calibration

The properties of the laser spot at the focal point determine how the particle will

behave in the trap. For a tightly focused beam, the light converges to a theoretical point

(RO description), but the width of the beam at the focal point is actually finite due to

diffraction effects. Equation (2.36) tells us that the force on the particle is proportional to

the intensity gradient, so the three-dimensional contour of the intensity profile is what ultimately determines the trapping force. Most lasers used in optical traps have a radial (or transverse) Gaussian profile (TEM$_{00}$ mode). This profile is usually maintained even as the beam is focused to a spot on the order of microns. In many cases, the axial intensity distribution is also modeled as having a Gaussian profile with a half-width some multiple *e* larger than the transverse direction, where *e* is the *eccentricity*. In most cases, *e* is a value of about three or more [31]. Since the distribution is narrower in the transverse direction (*e* > 1), the transverse trapping force is usually stronger than in the axial direction.

The approximately Gaussian intensity distribution leads to a linear force–distance relationship for the trapped particle for reasonably small displacements of the particle from the trap center. This suggests a Hookean spring model for the trapping force in all three dimensions, although we are typically only interested in the axial (z-direction) force component:

$$F_{trap}(z) = -g_z(z - z_0),$$
(2.37)

where g_z is the axial *trap stiffness*, and z_0 is the axial location of the trap center. The Hookean analogy simplifies the description of the trap by using just two parameters (in any one dimension) to quantify the trapping force. This relationship generally holds for displacements that are on the order of the spot size. Because of the eccentricity in the intensity distribution, the linear regime is often larger for the axial force. Beyond the linear regime, the force–distance relationship reaches a maximum and quickly falls off to zero. For force measurements, we are interested in the linear regime for simplicity of

calibration and in the data analysis. With values for g_z and z_0 for the trap, we can readily apply a simple force balance to the particle as it finds a new equilibrium location in response to external forces such as double layer repulsion.

To calibrate the trap, we observe the Brownian fluctuations of the trapped particle over time. The calibration procedure occurs far from any surface to ignore contributions from surface forces. The trajectory of the particle is governed by the (one-dimensional) Langevin equation:

$$m\frac{d^2 z}{dt^2} = -g_z(z - z_0) - d\frac{dz}{dt} + x(t),\qquad(2.38)$$

where m is the mass of the particle, d is the drag coefficient, and $x(t)$ is a random Brownian force. In most cases, the mass of the particle is small, so we can neglect the left-hand side (inertia term) of the Langevin equation. The exact motion of the particle is random, and the time-series solution requires a somewhat complicated Brownian dynamics simulation (which we have attempted and will show later). However, the equilibrium statistics of the particle's motion are relatively easy to find since the random force term is normally distributed around a zero mean. For a Hookean spring model of the trapping force, the trap stiffness is simply

$$g_z = \frac{kT}{s_z^2},\qquad(2.39)$$

where s_z^2 is the variance of axial position. The trap center is the peak of the distribution

and is equal to the mean axial position:

$$z_0 = \langle z \rangle. \tag{2.40}$$

With a calibrated method of detecting axial position, like EWLS, we can in turn

calibrate the optical trap and use it as a sensitive force measurement device. The details

of how force is measured using a gradient optical trap and EWLS are described in the

following section.

CHAPTER 3
DESCRIPTION OF THE TECHNIQUE

3.1 Apparatus

A schematic diagram of the experimental setup is shown in Figure 3-1.
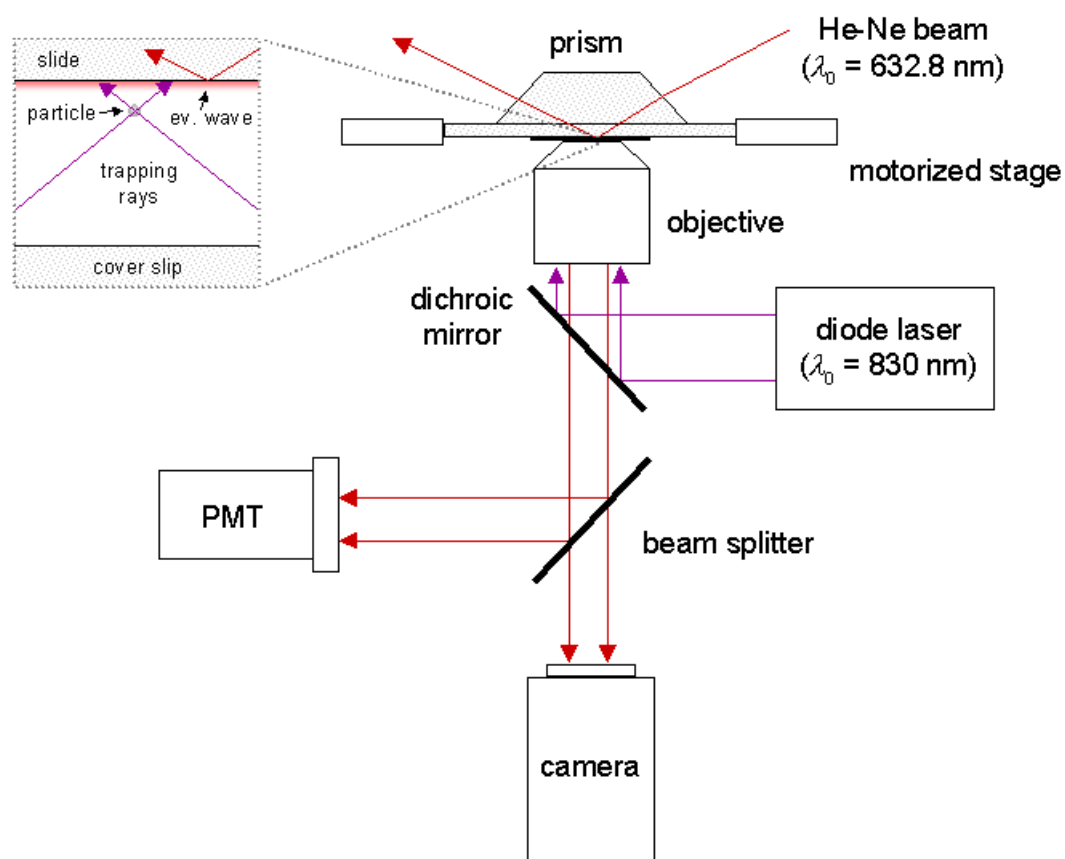
Figure 3-1. Schematic of the experimental apparatus.

The optical trap is a Cell Robotics LaserTweezers 100 which employs a 100 mW diode laser in the near infrared (I_0 = 830 nm). The trap housing is mounted in the epifluorescence port of a Nikon TE300 inverted microscope. The trapping beam is collimated and slightly overfills the rear opening of a Nikon 100× oil immersion objective (plan fluor, 1.3 NA) and is focused to a diffraction-limited spot within the fluid cell. The particle suspension is placed upon a pre-cleaned glass microscope slide (75 × 25 × 1 mm) and enclosed with a coverslip (25 × 25 × 0.13 mm). With the sample mounted to a three-axis motorized stage (Ludl Electronic Products), the objective lens is optically coupled to the glass coverslip with index matching oil (n = 1.515 at 23°C).

The evanescent wave is formed by directing a Melles Griot 35 mW He–Ne laser beam (I_0 = 632.8 nm, linearly polarized) into the 45° hypotenuse face of a BK–7 glass (n = 1.515 at 632.8 nm) dove prism, which is optically coupled to the glass slide with index matching oil. The He–Ne beam angle is precisely positioned with a rotation stage that is accurate to within 0.1°. This allows the evanescent wave penetration depth, b^{-1}, to be adjusted by varying the incident angle of the beam, as indicated by equation (2.20). A fraction of the scattered intensity from a particle near the glass slide is collected by the objective, and the image is visualized using a color CCD camera and a dedicated monitor. The magnitude of the scattered intensity is measured by a side-on photomultiplier tube (PMT; Oriel Instruments) mounted to the side port of the microscope. The PMT is fitted with an adjustable iris (typically forming a 1 mm diameter aperture) and bandpass filter (633 ± 2 nm) which isolates the scattered light from the trapped particle. The PMT signal is sent to a current pre-amplifier where it is electronically averaged by a 150 ms time constant RC circuit (low-pass filter) and then digitally sampled by a National Instruments

12-bit data acquisition board. The time series intensity data are saved to a PC file for later analysis.

3.2 Procedure

The following procedure was used for nearly all measurements performed over the course of this work. Particle solutions were prepared using Barnstead Nanopure ultrafiltered water (18.2 MΩ-cm resistivity). Silica microspheres were purchased from Geltech as dry powders and suspended in electrolyte solutions at low particle densities (~10^5 particles/mL). A similar density of 9.14 ± 1.24 μm diameter polystyrene microspheres (Polysciences) served as gap spacers. All solutions were prepared the day of an experiment to limit contamination. The solutions were each sonicated for one hour to break up particle aggregates and then agitated briefly with a touch mixer just prior to an experiment to resuspend settled particles.

A small amount (~10 μL) of the particle suspension was placed on the center of the glass slide and overlaid with a pre-cleaned glass coverslip. Excess solution was withdrawn from the slide using bibulous paper. The edges of the coverslip were then sealed using a minimum amount of insoluble silicone vacuum grease to prevent the liquid from evaporating during the course of the experiment. With the sample mounted, a single diffusing silica sphere was isolated in the field of view of the microscope and the optical trap was activated to confine the particle in the fluid gap. The He–Ne laser was activated at least 30 min prior to any measurements to ensure stability of the beam intensity. The particle was moved toward the glass slide surface until it began to scatter light from the evanescent wave. The incident angle of the He–Ne beam was adjusted to a value exceeding the critical angle (61.6°) for total internal reflection. The penetration

depth, b^{-1}, for these experiments ranged from 150 to 230 nm. A mirror mounted to a precision rotation stage (0.1° increments) adjusted the angle of the beam. The stage angle depended on the geometry of the system, but was calculated using equation (2.30). Shorter depths offer better distance resolution whereas larger depths lead to a measured signal and provide information about movements made farther from the slide surface. The lateral position of the beam was also adjusted to maximize the scattered intensity.

With the He–Ne beam properly aligned, the particle was moved away from the glass slide surface to a position where only background levels of intensity were measurable (several microns from the slide surface). A program was written in LabVIEW (National Instruments) to sample PMT measured intensities at varying positions from the surface. At each step in the scan, the program acquired an adjustable number of intensity samples (~10^4 to 10^5) at an adjustable rate (~2 to 50 kHz), recorded the data to a file, and moved to the next position toward the slide surface in adjustable increments (~10 to 30 nm). This process was repeated until the particle was as near to the surface as possible with the optical trap. The measurement procedure was repeated several times for the same particle–solution system in order to assess the quality and reproducibility of the data. The glass slides were discarded following an experiment, and each new particle–solution sample was mounted on a new glass slide.

3.3 Data Analysis

3.3.1 Signal Processing

The actual voltage signal obtained by the data acquisition system is not strictly proportional to the scattering intensity from the particle, $I(t)$, used in the above analysis. This is because the measured signal is persistently affected by a background intensity

level and uncorrelated (white) noise. An RC circuit associated with the pre-amplifier also filters the signal by removing high frequency fluctuations.

For typical experimental conditions, noise contributes less than 5% of the total signal magnitude, but accurate correction for this small noise is important for calibration of the optical trap and subsequent force measurements. Fortunately, most contributions to the total noise can be isolated. The first noise contribution is the fluctuating background intensity, $I_B(t)$, due to scattered light from surface irregularities and the residual background reading from the PMT. The second source is known as "shot noise," $I_S(t)$, where the discrete number of photons incident on the photodetector (described mathematically as a Poisson process) contributes to a distribution of measured intensities around a mean value. Assuming intensity contributions to be additive, the total measured intensity at some instant in time is

$$I_T(t) = I(t) + I_B(t) + I_S(t).$$ (3.1)

The mean background intensity, $m_B \equiv \langle I_B \rangle$, is measured when the particle is far enough from the surface as to not scatter the evanescent wave. This allows the correction of the subsequent positions using the background-corrected intensity, $I_C(t)$:

$$I_C(t) \equiv I_T(t) - m_B = I(t) + I_N(t)$$ (3.2)

where $I_N(t) \equiv I_S(t) + I_B(t) - m_B$ is the total fluctuating noise contribution. Because

$\langle I_S \rangle = 0$, then $\langle I_C \rangle = \langle I \rangle = m$.

Assuming that fluctuations in $I(t)$ and $I_N(t)$ are uncorrelated, the autocorrelation

function of $I_C(t)$ is given by

$$G_C(t) \equiv \langle I_C(t+t)I_C(t) \rangle - m^2 = G_I(t) + G_N(t) \tag{3.3}$$

where $G_I(t) \equiv \langle I(t+t)I(t) \rangle - m^2$ and $G_N(t) \equiv \langle I_N(t+t)I_N(t) \rangle$. The relaxation time of

the fluctuations in $I_N(t)$ is much smaller than that of $I_C(t)$, which allows a substantial

amount of noise to be removed by the RC filter without corrupting the desired lower

frequency fluctuations of $I(t)$. In most cases, the time constant, t_f, of the RC filter was

set to 150 ms. The autocorrelation function of the filtered signal is given by

$$G_f(t) = \int_{-\infty}^{\infty} \frac{G_I(t')}{2t_f} e^{-|t-t'|/t_f} dt' + s_N^2 e^{-|t|/t_f} \tag{3.4}$$

where s_N^2 is the variance of the filtered noise [32]. Extracting force data from the

measurements using equation (3.4) requires a model for the fluctuating particle position.

Our approach is to model these fluctuations as Brownian motion in a potential energy

well.

3.3.2 Brownian Motion in a Potential Energy Well

The goal of the measurements is to simultaneously extract force–distance profiles for the conservative (static) forces, which depend only on separation distance, and non-conservative (dynamic) forces, which depend on the position and velocity of the particle. The conservative forces are characterized by the gradient of the potential energy, $\mathbf{f}(z)$:

$$F(z) = -\mathbf{f}'(z). \qquad (3.5)$$

The simplest example of a non-conservative force is the low Reynolds number viscous force, which is directly proportional to the particle velocity:

$$F_{drag}(z) = -\mathbf{d}(z)\frac{dz}{dt} \qquad (3.6)$$

where $\mathbf{d}(z)$ is the drag coefficient in the direction normal to the flat surface. For large separations, $\mathbf{d}(z)$ approaches the Stokes' law value, $\mathbf{d}(z) = 6\mathbf{ph}a$, where $\mathbf{h}$ is the fluid viscosity and a is the particle radius. However, for separations on the order of several particle radii and less, there is sufficient viscous coupling with the solid wall such that the drag coefficient becomes a strong function of separation:

$$\mathbf{d}(z) = 6\mathbf{ph}a\mathbf{l}(z) \qquad (3.7)$$

where $\boldsymbol{l}(z)$ is a correction factor that depends on separation distance. For particle

motion in a Newtonian fluid with no-slip boundary conditions, $\boldsymbol{l}(z)$ has an analytical

solution that becomes infinite as the separation vanishes, and tends to unity (as in Stokes'

law) for infinite separation. This result was first derived by Brenner [33] in 1961.

In these experiments, the particle's range of motion is limited by a potential

energy well created by the optical trap alone or together with the surface. The probability

density of a Brownian particle in a potential energy well can be described by the one-

dimensional Fokker–Planck equation,

$$\frac{\partial p(z,t \mid z',0)}{\partial t} = \frac{\partial}{\partial z}\left[\frac{\boldsymbol{f}'_{tot}(z)}{\boldsymbol{d}(z)}p(z,t \mid z',0) + \frac{kT}{\boldsymbol{d}(z)}\frac{\partial p(z,t \mid z',0)}{\partial z}\right], \qquad (3.8)$$

where $p(z,t \mid z',0)dz$ is the probability of finding the particle between z and $z+dz$ at

time t given the particle was at position z' at time zero, $\boldsymbol{f}_{tot}(z)$ is the total potential

energy, k is Boltzmann's constant, and T is the absolute temperature. In the case of a

Newtonian fluid, the calibration and measurement procedures assume the validity of

equation (3.8) for the trapped particle. The primary assumptions underlying this equation

are the validity of equation (3.6) (viscous force proportional to velocity) and a fast

relaxation of velocity fluctuations relative to the time scale of interest. Based on a root

mean square velocity, $v_{rms} = \sqrt{2kT/m}$, the Reynolds number is estimated to be less than

0.004, validating the Stokes flow assumption. The velocity relaxation time, equal to

$m/\boldsymbol{d}$, is estimated to be less than 10^{-7} s for typical measurements. Also, the persistence

length associated with the velocity fluctuations, estimated by $v_{rms} \cdot m/\boldsymbol{d}$, is less than 0.5

nm, which indicates that any persistent motion of the particle due to a finite relaxation time of the velocity can be neglected.

Solving equation (3.8) for the stationary probability density yields

$$p_s(z) = \frac{e^{-f_{tot}(z)/kT}}{\int\limits_{-\infty}^{\infty} e^{-f_{tot}(z')/kT} dz'},$$
(3.9)

which is a statement of Boltzmann's law. A key property of equation (3.9) used in the force measurements is that, because $p_s'(z) = -p_s(z)f_{tot}'(z)/kT$, $f_{tot}(z)$ and $p_s(z)$ share extrema with respect to z. In other words, the maximum in the measured position histogram and the minimum in the total potential profile occur at the same location. The autocorrelation function of the particle position, given by

$$G_z(t) \equiv \langle (z(t+t) - \langle z \rangle)(z(t) - \langle z \rangle) \rangle = \int\limits_{-\infty}^{\infty} dz' \int\limits_{-\infty}^{\infty} dz\, p_s(z')p(z,t\mid z',0)zz' - \langle z \rangle^2, \quad (3.10)$$

can also be obtained from equation (3.9) and the solution to equation (3.8).

In the special case where $f_{tot}(z)$ is approximately parabolic of the form

$f_{tot}(z) = \frac{1}{2}f_{tot}''(z)(z - z_p)^2$, centered around position z_p, then

$$p_s(z) = \left(\frac{f_{tot}''(z)}{2pkT} \right)^{1/2} \exp\left[-\frac{f_{tot}''(z_p)(z - z_p)^2}{2kT} \right]$$
(3.11)

from which the mean position, $\langle z \rangle = z_p$, and the variance, $\boldsymbol{s}_z{}^2 = kT/\boldsymbol{f}''_{tot}(z)$, can be obtained. Furthermore, when $\boldsymbol{d}(z)$ is nearly constant and approximately equal to $\boldsymbol{d}(z_p)$ over the local range of fluctuations, then equation (3.8) can be solved and introduced into equation (3.10) to yield

$$G_z(\boldsymbol{t}) \equiv \boldsymbol{s}_z{}^2 e^{-|t|/t_c} \tag{3.12}$$

where $\boldsymbol{t}_c = \boldsymbol{d}\boldsymbol{s}_z{}^2/kT = \boldsymbol{d}/\boldsymbol{f}''_{tot}(z)$ is the characteristic relaxation time of the fluctuating position. We show in the Appendix that equation (3.12) remains a good approximation even when the potential well is slightly skewed and $\boldsymbol{d}^{-1}(z)$ (or the particle diffusivity) varies linearly with position.

Because we are directly measuring the intensity rather than the particle position, we need to relate the statistical properties of the two variables using equation (2.19). From equations (2.19) and (3.11), the mean intensity, $\boldsymbol{m}$, and variance, $\boldsymbol{s}_I^2$, are given by

$$\boldsymbol{m} = \int_{-\infty}^{\infty} I(z) p_s(z) dz = I_0 e^{-bz_0} e^{b^2 s_z^2/2} \tag{3.13}$$

and

$$\boldsymbol{s}_I^2 = \int_{-\infty}^{\infty} I^2(z) p_s(z) dz = \boldsymbol{m}^2 \left(e^{b^2 s_z^2} - 1 \right), \tag{3.14}$$

respectively. Moreover, it can be shown that the autocorrelation function of intensity is given by

$$G_I(t) \equiv \langle I(t+t)I(t) \rangle - m^2 = m^2 \left[\exp\left(b^2 G_z(t) \right) - 1 \right] \qquad (3.15)$$

where $G_z(t)$ is given by equation (3.12).

Equation (3.15) is the key result to be used in the calibration of the trap and in the measurement of dynamic forces, which requires estimation of s_z^2 and t_c from the measured autocorrelation function of intensity. However, the actual signal is represented by equation (3.4) due to the low-pass filter. Upon introducing the series expansion of the exponent in equation (3.15) into the integral in equation (3.4), we find

$$G_f(t) = G_I(t) + e^2 m^2 e^{b^2 G_z(t)} b^2 G_z(t) \left[1 + b^2 G_z(t) \right] - \left[e m^2 e^{b^2 s_z^2} b^2 s_z^2 + s_N^2 \right] e^{-|t|/t_f} + O(e^3) \qquad (3.16)$$

where $e \equiv t_f / t_c$ is the ratio of the filter time constant to the relaxation time of particle fluctuations. Because t_c is typically at least one order of magnitude larger than t_f, the higher-order terms in equation (3.16) are safely dropped.

3.3.3 Calibrating the Optical Trap

Since the stiffness of the optical trap may be sensitive to experimental conditions, an independent calibration is performed for each experimental run. For separation distances where the surface forces are negligible, the trapping force is the only

conservative force acting on the particle. The restoring force due to the trap is approximately linear for axial displacements on the order of a particle diameter:

$$F_{trap}(z) = -\boldsymbol{g}_z(z - z_0) \tag{3.17}$$

where $\boldsymbol{g}_z$ is the axial trap stiffness and z_0 is the trap center (neither is known *a priori*). Since the location of the particle is specified by the separation distance, z, the convention is adopted to define the trap center as the equilibrium *separation distance* of the particle in the absence of surface forces. This means that the actual location of the trap *focal point* and the so-called "trap center" are offset by a distance approximately equal to the particle radius, a. A linear model for the trapping force implies a simple harmonic potential energy profile; integrating equation (3.17) with respect to separation distance gives

$$\boldsymbol{f}_{trap}(z) = \frac{\boldsymbol{g}_z}{2}(z - z_0)^2 \tag{3.18}$$

which is the potential energy relative to the local minimum value at z_0.

If no other forces are present, then $\boldsymbol{f}_{trap}(z) = \boldsymbol{f}_{tot}(z)$, and the stationary density is simply the Gaussian distribution given in equation (3.11). The trap stiffness, $\boldsymbol{g}_z = \boldsymbol{f}''_{trap}(z)$, and the trap center, z_0, are determined by the first two statistical moments (i.e., the mean, $\langle z \rangle$, and variance, $\boldsymbol{s}_z^2$) of the particle's position within the trap. This calibration is performed over a range of trap positions far from the surface where only the

trapping force is significant and the position variance, s_z^2, is a constant and equal to

kT/g_z. The position variance, s_z^2, is determined at each calibration position by fitting

equation (3.16) to the measured autocorrelation function by non-linear least-squares

regression, using s_z^2, t_c, and s_N^2 as fitted parameters. This provides a precise, noise-

corrected estimate of the trap stiffness, g_z, and ultimately the drag coefficient, $d(z)$.

The calibration is performed by at known trap positions $\{z_{0,j}\}$ initially defined

relative to an arbitrary zero point. The calibration procedure also determines the intensity

at zero separation, $I_0 = I(z = 0)$, on this scale. This can be estimated by rearranging

equation (3.13) to relate I_0 to z_0 and the measured mean intensity, m, then taking the

appropriate average from the measurements:

$$\ln I_0 = \frac{1}{n} \sum_{j=1}^{n} \left(b z_{0,j} + \ln m_j - \frac{b^2}{2} \frac{kT}{g_z} \right) \tag{3.19}$$

where m_j is the measured mean intensity at trap position $z_{0,j}$.

3.3.4 Measuring Static Forces

Once the optical trap is calibrated, it is used as a sensitive force transducer. Of

particular interest are the DLVO-type forces which include the screened electrostatic (i.e.,

double layer) and van der Waals interactions of the particle with the flat surface. These

are considered to be static forces because they are conservative over the entire range of

separation distances and are insensitive to the particle's Brownian motion. In the

calibration region, the static forces are negligible due to the relatively large separation

distance; here, only the force due to the trap is significant. However, as the particle

approaches the surface, the surface forces begin to perturb the equilibrium position of the

particle within the trap. Assuming that the potential energy contributions from the trap,

$\boldsymbol{f}_{trap}(z)$, and particle–surface interactions, $\boldsymbol{f}(z)$, are additive, the total potential energy of

the particle is

$$\boldsymbol{f}_{tot}(z) = \boldsymbol{f}(z) + \boldsymbol{f}_{trap}(z). \tag{3.20}$$

The local minima of $\boldsymbol{f}_{tot}(z)$ represent separation distances where there is a *stable* balance

between the trapping force and surface forces such that

$$\boldsymbol{f}'_{tot}(z_p) = 0 = -F(z_p) + \boldsymbol{g}_z(z_p - z_0). \tag{3.21}$$

Therefore, once z_p is identified, the force can be calculated directly from

$$F(z_p) = -F_{trap}(z_p) = \boldsymbol{g}_z(z_p - z_0) \tag{3.22}$$

for any trap position. The details of the procedure for estimating z_p from the raw

intensity measurements are presented elsewhere [13]. Briefly, z_p is obtained from the

minimum of a fourth-order polynomial fit to the negative logarithm of the measured

distribution of positions, i.e., $-\ln p(z(I)) \propto \boldsymbol{f}_{tot}(z)$. By moving the location of the trap

center, z_0, toward the surface in small increments, the interaction force as a function of

separation distance is readily determined from an equilibrium force balance at each new location. A smoothly varying force–distance profile can be integrated numerically to yield an estimate of the potential energy,

$$\boldsymbol{f}(z) = \int_z^\infty F(z_p)\,dz' , \qquad (3.23)$$

over the same range of separation distances. This offers a comparison with potential energy data produced by TIRM measurements.

3.3.5 Measuring Dynamic Forces

In order to determine the drag force as a function of separation distance, we again examine the autocorrelation function at each new trap position. A key assumption is that equation (3.12) and, consequently, equation (3.16) remain good approximations even when particle is within a potential energy well created by the trap and the surface together. This requires that the particle fluctuations are reasonably symmetric about the potential energy minimum and the drag coefficient does not deviate largely over the range of fluctuations from its value at z_p. A Taylor series expansion of the potential energy centered at the most probable position, z_p, yields

$$\boldsymbol{f}_{tot}(z) - \boldsymbol{f}(z_p) \approx \frac{\boldsymbol{f}''(z_p)}{2}(z - z_p)^2 \qquad (3.24)$$

where we have noted that $f'(z_p) = 0$ at equilibrium. Equation (3.24) assumes that the

total potential profile, $f_{tot}(z)$, is approximately harmonic (parabolic in shape) near z_p

such that the *effective stiffness*, combining trap and surface force effects, is

$$g_{z,eff}(z_p) = f''(z) = g_z - F'(z_p). \tag{3.25}$$

Equation (3.25) shows that repulsive surface forces that decrease with separation distance

(i.e., $F(z_p) > 0$ and $F'(z_p) < 0$) enhance the effective stiffness and narrow the total

potential energy well. Conversely, weakly attractive forces ($F(z_p) < 0$, $F'(z_p) > 0$) tend

to decrease the effective stiffness and broaden the potential energy well. We also assume

that $d^{-1}(z)$ (or the particle diffusion coefficient) depends weakly and linearly on z over

the range of fluctuations to justify the use of equations (3.12) and (3.16) to estimate the

position variance, $s_z^2(z_p) = kT/g_{z,eff}$, and the relaxation time, $t_c(z_p) = d/g_{z,eff}$, as

functions of z_p. As with the calibration procedure, these parameters are estimated at

each trap location by first measuring $G_f(t)$, and using equation (3.16) to fit to the data

via weighted non-linear least-squares regression, with s_z^2, t_c, and s_N^2 as fitted

parameters.

3.3.6 Determining Absolute Separation Distances

　　As mentioned above, the measured separation distances using this technique are

initially expressed relative to an arbitrary reference point since we lack a direct estimate

of the intensity at zero separation distance. To determine absolute separation distances,

we compare the drag force data with theory such that the position offset can be inferred

from a fitting procedure. Whereas DLVO theory depends on several unknown parameters (the surface potential is often the most difficult to estimate for a particular system), the hydrodynamic drag far from the surface theoretically depends only on the particle radius, fluid viscosity, and absolute separation distance. This allows for a rather simple method of determining absolute separation distances using the measured drag force profile. Similar procedures of using the drag coefficient (or, equivalently, the apparent diffusion coefficient) as a means of determining absolute distances has been applied previously in TIRM measurements [9, 10].

All dynamic force data reported here were ascribed absolute distances determined from a fit of equation (3.7) to the data. Because our measured drag coefficient deviated significantly from equation (3.7) in the region of double layer overlap, we performed the fit using only data from larger distances where there the measured static force was near zero and the overlap of the double layers is negligible. Nevertheless, the large number of data points remaining at these larger separation distances provides a good estimate of the absolute separation distance.

CHAPTER 4
INITIAL FORCE MEASUREMENTS AND EVIDENCE OF INTERFERENCE
EFFECTS

4.1 Initial Static Force Experiments

This section summarizes the first set of static force measurements made using the

new technique. This study was intended to demonstrate the technique's accuracy for

measuring static interactions between a micron-sized particle and a flat glass plate.

Experiments were performed using 1.5 μm silica spheres suspended in solutions of

varying ionic strength. Since the characteristic distance of electrostatic interactions, the

Debye length, varies with the ionic content of the solution, this is a convenient way to test

the accuracy of the technique. As will be shown, however, the measurements produced

unexpected results that did not agree well with theoretical predictions. At first it was

thought that these measurements were accurate because they follow DLVO theory,

although the Hamaker constant required for such agreement was unusually high.

Regardless, the measured double layer repulsion agreed well with theory.

Following this study, further investigations eventually led to the hypothesis that

reflection effects at the glass–water interface might be influencing the experimental

results. This was verified by adjusting the entry point of the trapping beam to the

objective lens which would reduce or enhance this effect depending on the beam

placement. Additional studies using slides with reflective dielectric coatings further

showed that this was the source of the anomalous data. The details that lead to this

conclusion are presented in this chapter as well.

4.1.1 Static Force Results

In order to validate the technique experimentally, we chose to study a well-characterized system that could be described by classical DLVO theory. The simplest system we can consider is a spherical particle interacting with a flat plate immersed in an aqueous solution of known ionic strength. We chose silica microspheres because of their spherical shape, monodisperse size distribution, availability in the micron-size range, and tabulated material properties. Standard microscope glass slides were used as the test surfaces and were found to be reasonably smooth for experiments (surface roughness of about 2 nm RMS as measured by AFM). Solutions were prepared with NaCl added to ultra-purified water to a specified concentration. The ionic strength of the solutions was measured using a conductivity bridge. Using equation (2.19), we were able to specify several values for the Debye length, k^{-1}. The measured exponential force–distance relationship created by the overlapping double layers offers the most robust test of the technique's accuracy since the Debye length is only a function of the electrolyte concentration. Attractive forces due to van der Waals interactions are usually not measurable for most common systems of low ionic strength where the double layer forces dominate.

Measurements were made using 1.5 μm silica microspheres interacting with a soda-lime glass slide in solutions of varying NaCl concentration. We prepared solutions of 0.10, 0.18, and 0.40 mM NaCl in doubly distilled water (corresponding to three equal-spaced Debye lengths), each suspended with a low density of silica particles and polystyrene spacers ($\sim 10^5$ particles/dm^3). We made several runs of the same system to

assess repeatability of the data, and saved all data to PC files for later analysis using an

algorithm written in MATLAB. The details of the analysis are given in detail previously.

The applied trap potential is assumed to be harmonic, and we can demonstrate this

by looking at the position histograms generated by a trapped particle. Figure 4-1 is a

histogram plot for two different locations of the trap center.
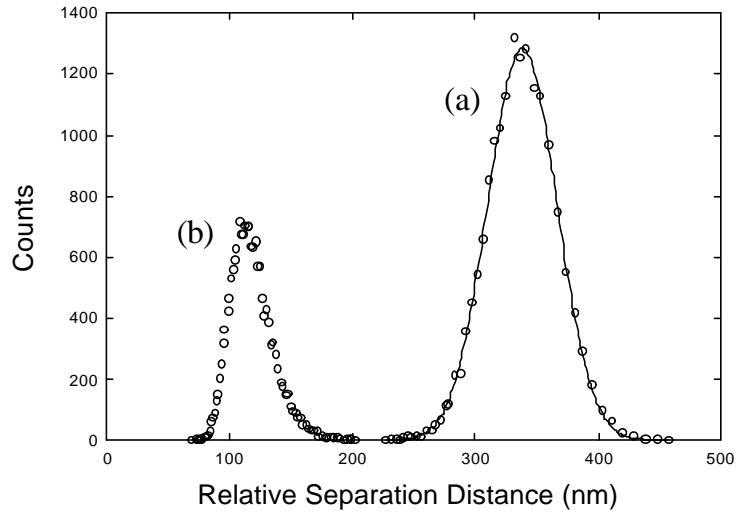
Figure 4-1. Position histograms of a particle trapped (a) far from and (b) near the plate surface.

Histogram (a) shows a trapped particle sufficiently far from the plate surface such that the

interaction forces are negligible. Fitting this histogram with a Gaussian distribution

function (solid line) shows a good agreement with the harmonic trap model for

displacements up to about 100 nm. From this data, we cannot tell if the model fails for

larger displacements within the trap since the particle does not naturally sample these

regions. Histogram (b) shows the same particle trapped much closer to the plate surface

where interaction forces become significant. Rather than having a Gaussian shape, the

distribution is now skewed to the right due to the presence of strong double layer repulsion.

The histograms in Figure 4-1 represent the collected data for a given location of the trap center. To calculate a complete force–distance profile, many such histograms are generated as the trap center is moved toward the plate surface. For each of these locations, a force balance is made at the peak of these distributions knowing the location of the trap center. The experimental force–distance profiles are shown in Figure 4-2.
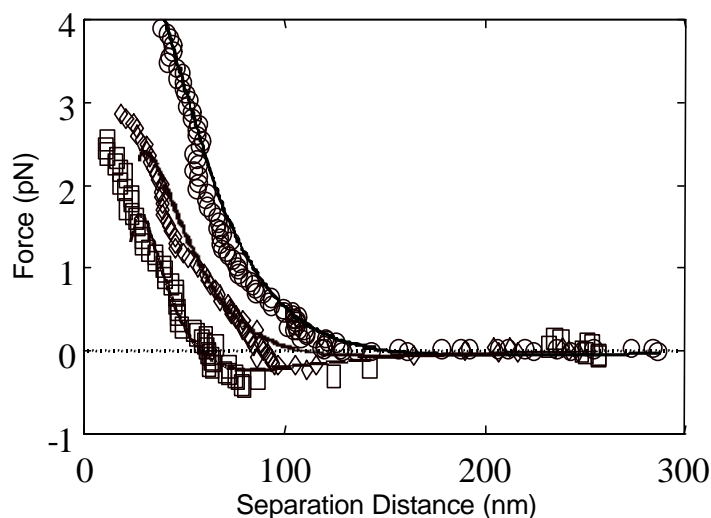
Figure 4-2. Experimental force–distance profiles for 1.5 μm silica near a glass slide. ($\bigcirc$ – 0.1 mM NaCl, $\diamondsuit$ – 0.18 mM NaCl, $\square$ – 0.40 mM NaCl)

The symbols in Figure 4-2 represent measured data points, and the lines are a DLVO theory fit generated from a Hogg–Healy–Fuerstenau (HHF) expression [18]. In all three measurements, there was good agreement between the expected Debye length and the observed decay constant of the data. However, there is an obvious region for the two higher electrolyte concentrations where the forces are attractive (negative), signifying the

existence of an unusually deep secondary energy minimum. Note that the reasonable fit of the data using the HHF expression is only achieved by choosing a relatively high value for the Hamaker constant (for a silica–water–glass system). In this form of the DLVO theory, the van der Waals forces are calculated using equation (2.16). This expression for the van der Waals energy does not assume retardation effects, however, which will be significant above separations of about 10 nm [7]. If we use a more rigorous Lifshitz expression for the van der Waals interactions, the predicted attractive force will be much lower for our system than the measurements in Figure 4-2 would indicate, over the same range of separation distances. In effect, a rigorous version of DLVO theory suggests that our system should generate purely repulsive interactions over the range of separation distances and concentrations measured.

4.1.2 Discussion of Static Force Results

It is clear that the measured attractive forces are unusually large for these systems, so we need to consider some reasonable explanations for the discrepancy. One possible explanation is to assume that our measurements of large attractive forces are legitimate and that the theory somehow does not apply in this case. This explanation is tempting, but is probably presumptuous since a large number of studies—many using SFA—have shown the Lifshitz theory to be very accurate [4, 34]. Another possible explanation would be the presence of *depletion interactions*, which can induce significant attractive forces, but this is unlikely since it requires the addition of small particles or long-chain molecules to the solution in sufficient concentration.

If we assume that DLVO theory is accurate, our attention turns to the assumptions about optical trap. It is possible that the trap does not act as a linear spring over a large range of axial displacements from the trap center, as it is assumed. We might infer from

our measurements of strong attractive forces that the trap is somewhat weak in the reverse direction (i.e., opposite to the direction of beam propagation) as opposed to the forward direction. This may allow the particle to be disrupted from the trap more easily if there are moderate attractive forces. One argument against this view is that Lifshitz theory predicts van der Waals attractive forces to be significant only within 100 nm, and even then these forces are very small for a micron-sized particle (recall that van der Waals forces scale with particle radius). Although our force–distance profiles in Figure 4-2 reflect relative separation distances, clearly there appear to be strong attractive interactions occurring at separations much beyond 100 nm. For these unusually large attractions to occur, even with weak reverse trapping, there would still need to be a significant attractive force that extends significantly beyond 100 nm. This hypothesis is not supported by Lifshitz theory.

Thus far, our attempts to explain the experimental force data have been inadequate. It appears as though we are accurately measuring double layer repulsion (note the 0.1 mM data in Figure 4-2), but the relatively strong attractive forces seemingly defy explanation using reasonable arguments. There are cases in the literature where attractive forces appear to be higher than usual, and we might consider our measurements to support these findings. Of note are results from recent experiments by Velegol et al. [35, 36] using *differential electrophoresis* where the electric field required to separate two particles of differing surface charge, loosely bound in mutual secondary minima, was found to be much higher than that predicted by DLVO theory. A possible explanation for this effect, however, might be that the applied separation force is not well known in electrophoresis. The resolution of force in such a study would be far less than that found

using an optical trap. This experimental result alone is not enough to bolster our

findings.

The lack of an obvious explanation for the poor agreement between theory and

data led us to look at the data more carefully. Based on DLVO theory and an accurate

description of the trapping energy, we can simulate an experiment and determine how the

data should appear for a certain particle–surface system. Using the overall potential

energy for the particle as the sum of DLVO-type interactions and trap contributions, we

can use Boltzmann's equation to predict how the histograms should appear as we move

the trap center toward the plate surface. These histograms can be difficult to compare

with a large set of experimental histogram data, so it is often useful to compare the

statistics of these distributions. The raw data sampled by the data acquisition program is

measured in terms of a voltage level that is proportional to the scattered intensity of the

particle, so it is convenient to analyze the mean and variance intensity profiles as the

particle approaches the surface. This is a convenient way of comparing the measured

data with predicted quantities. It is a simple matter to calculate the expected intensity

mean and variance from the theoretical distributions by first using the EWLS relation in

equation (2.32) to convert distances to intensities, and then integrating the curves to

generate the first two statistical moments. A comparison of the mean intensity profiles is

shown in Figure 4-3.
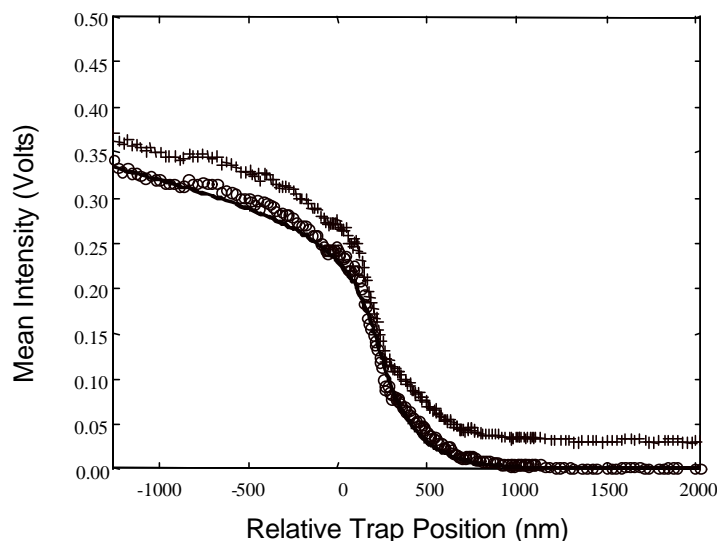
Figure 4-3. Experimental and theoretical mean intensity versus trap position for 1.5 μm silica sphere. (0.1 mM NaCl solution; + – raw data, ○ – background level subtracted, solid line – model prediction)

With the background level subtracted, the mean intensity profile appears to follow the model prediction (solid line) very well. The plot clearly shows an exponential rise of the average intensity as the trap center is moved toward the surface (leftward on this plot). The exponential rise is then followed by a curve inflection and finally a leveling of the intensity. We can interpret this data as an indication of repulsive forces for smaller separations because the curve deviates far below an exponential dependence. In the absence of surface forces, the intensity data should vary exponentially until contact. We can divide the curve into two distinct regions: a calibration region where the surface forces are negligible (exponential rise of mean intensity), and a measurement region where surface forces are significant to oppose the trapping force and displace the particle from the trap center (portion of the curve to the left of the inflection point).

The data shown in Figure 4-3 corresponds to the force curve shown Figure 4-2 for a 1.5 *m*m silica sphere in 0.1 mM NaCl. In both plots, the data is consistent with DLVO theory predictions, showing a purely repulsive interaction over the range of measurements. Unfortunately, this agreement is not easily reproducible. In most cases, there is significant deviation from DLVO theory predictions. Without having to rigorously analyze the data to produce force–distance profiles (the ultimate end-result of measurement), the raw data of mean intensity versus trap position can suggest if the measured data follows DLVO theory predictions or not. In many cases, the measured profile of the mean intensity has certain unexpected features. A typical example is shown in Figure 4-4.
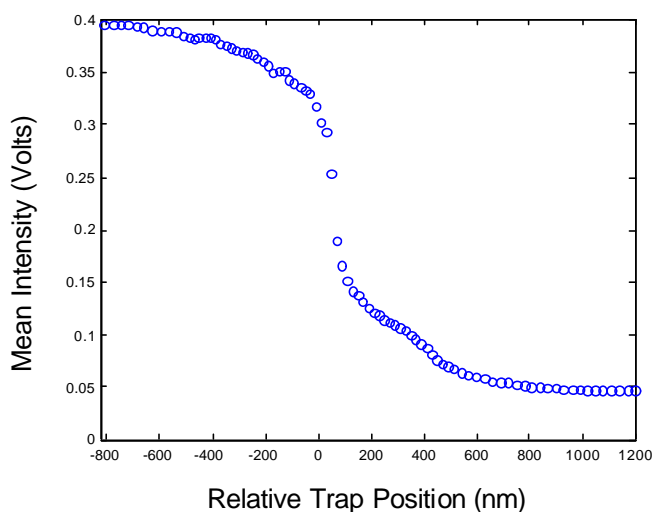

Figure 4-4. Experimental mean intensity versus trap position for a 1.5 *m*m silica sphere.

In comparison to the plot in Figure 4-3, the data shown in Figure 4-4 shows two unique features. First, there is an unusual "bump" in the data occurring in the exponential rise portion of the data (from about 200 to 400 nm). This feature cannot be explained using

DLVO theory. Second, the maximum slope of the curve is so extreme that the curve appears to be nearly discontinuous. Since the data depict discrete 20 nm movements of the trap center toward the plate surface, this discontinuity would appear to be due to an unusually strong attractive force. Most of the static force measurements using colloidal particles ranging from 0.5 to 5.0 mm in diameter have shown these effects to varying degrees.

In order to analyze this data, we had to account for these unexpected features. The simplest explanation seemed to be that the small "bump" was due to some artifact that did not affect the force measurement, and that the discontinuity in the mean intensity was due to a strong attractive force. As such, we could disregard the data to the right of and including the "bump," and perform a calibration using a smoothly varying portion of the exponentially varying region. Notice that the force data shown thus far have been over a limited range of separation distances, up to about 300 nm. This is primarily due to the presence the "bump" where we have omitted anomalous data. Isolating the cause of these unexpected features has been extraordinarily difficult. These effects appear to be independent of the sample preparation and experimental conditions. Fortunately, though, a reasonable explanation was discovered for this unexpected result. This is the subject of the sections to follow.

4.2 Effect of Trapping Beam Alignment

An additional adjustable parameter not considered in the previous experiments is the position of the trapping laser beneath the objective lens. The LaserTweezers 100 unit is designed to simply slide into place within the epifluorescence port of the microscope without end-user adjustment. It was determined that the position of the trap along the

guide rail was important only after the trap was inserted and removed from the

microscope (before and after experiments) with greater regularity. Only then was the

connection drawn between the quality of the measured data the location of the trapping

unit. This observation led to the conclusion that there may be significant reflection of the

trapping beam at the glass–water interface. It is not intuitively obvious that this should

be the case since the interface should reflect a minute fraction of the total beam intensity

(<1%). Nonetheless, experiments were run to deduce the dependence of the trapping unit

location within the microscope, which affects the entry point of the beam to the back

aperture of the objective lens. The results of these studies are discussed below.

A schematic of the optical trapping unit (Cell Robotics LaserTweezers 100)

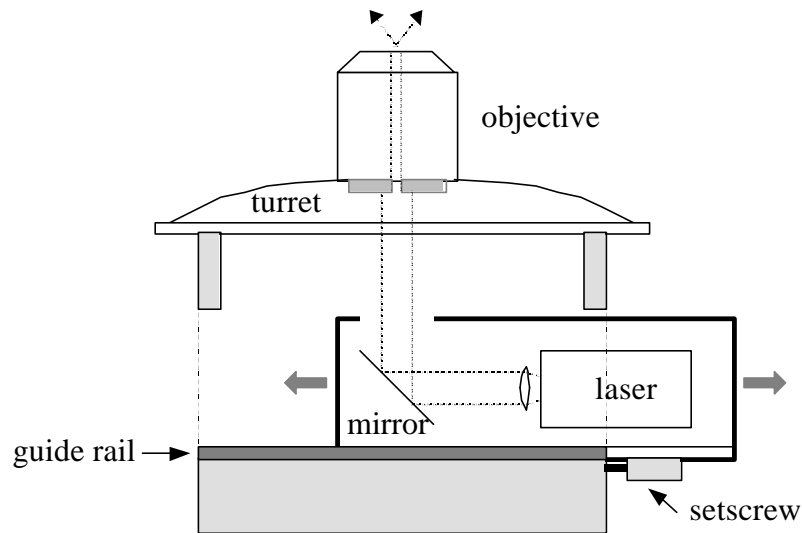placed within the microscope is shown in Figure 4-5.

Figure 4-5. Schematic of LaserTweezers unit placed within the microscope.

The trapping laser is contained within a small plug-in unit that is specifically designed to fit within the epifluorescence port of an inverted microscope. The unit collimates an infrared beam and reflects the light to the rear opening of a high numerical aperture objective. The collimated beam intentionally overfills the rear opening (by about 20%) such that the marginal rays are occluded; this significantly improves the axial trapping strength. The entire unit slides into position on a dovetail-shaped rail that restricts movements along one axis (as indicated by the arrows in Figure 4-5). A small setscrew is used to fix the position of the unit along this axis. Ideally, the beam axis should be concentric with the axis of the objective. This corresponds to the maximum power of the beam exiting the objective and the maximum trapping force.

The most precise way of aligning the trap is to measure the light intensity emitted from the objective. Since the laser operates in the near-infrared (IR) spectrum, the beam can be imaged using an IR-sensitive card or a CCD camera. The properly aligned position will yield a maximum intensity spot. A more practical approach is to align the unit using a trapped particle as a guide. As the trapping unit slides along the guide rail, the particle will also show small micron-scale movements along one axis. The details of this method are somewhat difficult to describe and require hands-on experience. Essentially, the method involves correlating the particle's movements to the ideal location of the trapping unit within the microscope. Although difficult to describe here, this method is far more convenient than measuring the beam output each time.

The so-called "artifacts" in the initial force measurements appeared be attributable to a yet unknown physical phenomenon since the particle was visually observed to make unexpected movements as it neared the flat plate surface, corroborating the trends seen in

the anomalous data. Recall that this particularly strange observation was shown in the

region where the intensity jumped discontinuously as a function of trap position (see

Figure 4-4). Here it was noted that the particle became somewhat unstable within the

trap and moved almost erratically towards and away from the surface. This was

qualitatively observed under the microscope as large variations in the intensity.

Experimentally, the sampled data clearly showed a larger than expected peak in the

intensity variance, s_I^2, than would be predicted by DLVO theory. This observation leads

to two possible explanations: either the attractive surface forces sufficiently broaden the

overall potential profile, or the trap itself is weakened significantly in this region. If we

are reasonably confident that DLVO theory is accurate for this system, we should

naturally suspect that the trap is responsible the unexpected results. At this point, it is not

as important to describe a precise mechanism for this result (to be addressed in a later

section) as it is to show the effect of beam alignment on the data.

To test the effect of the beam alignment, intensity mean and variance plots were

generated for different locations of the trapping unit beneath the objective.

Representative mean intensity plots are shown in Figure 4-6.
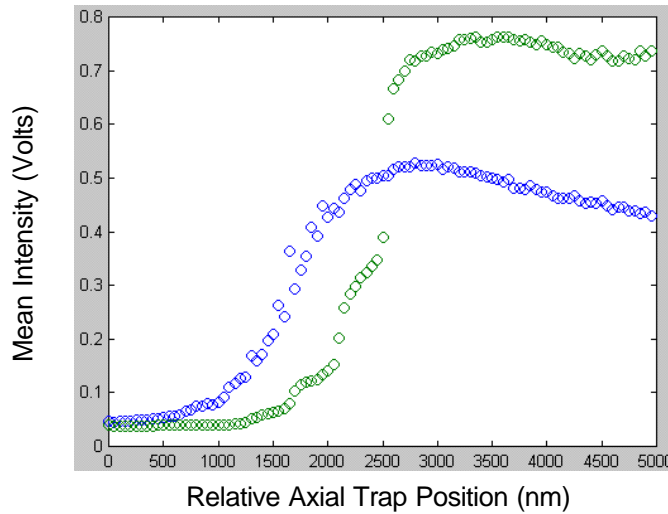
Figure 4-6. Mean intensity versus trap position for two locations of the trapping unit.

The data show an obvious dependence on beam alignment. Curiously, "anomalous" data results when the beam is precisely centered beneath the objective. Conversely, when the beam is moderately *off-axis*, (i.e., intentionally misaligned) the data are consistent with DLVO theory predictions. This result is both exciting and frustrating: we have implicated the alignment of the trap as the cause of our inaccurate measurements, but the solution to this problem makes little sense. Why should an aligned beam, and hence a well-formed trap, lead to inaccurate measurements? This is the subject of the next section.

While it is not yet described why an off-axis beam gives improved results, it is a useful pragmatic approach that significantly improves experimental static force measurements. Unfortunately the measurements are extremely sensitive to the beam location beneath the objective, so even minor movements of the trapping unit can influence the data greatly. This represents a significant obstacle to achieving repeatable measurements using this system.

4.3 Reflection Effects in Optical Trapping

That an aligned beam would give the most unusual results while a misaligned beam would yield agreement with theory seems counterintuitive. The most rational explanation would be that the description of the optical trap is inadequate in some fundamental way. One explanation previously conjectured for this discrepancy is that the presence of the flat plate in proximity to the beam focus somehow perturbs the electromagnetic field distribution. Since the beam propagates normal to the plate, it is possible that effects due to beam reflection could be responsible for a more complicated field distribution as the particle nears the surface.

4.3.1 Standing Wave Trapping

Interestingly, there is a related technique called *standing wave trapping* (SWT) developed by Zemánek and co-workers [39, 40]. This technique intentionally generates interference between the incoming trapping beam and its reflection at the plate surface, thereby forming a standing wave that confines micron-sized particles near the plate surface. Rather than generating a single focal point to which a particle is attracted, the standing wave is comprised of several periodic intensity maxima that can collect several particles at regular intervals of one-half the wavelength of the light, $\lambda/2$. Sufficient reflection of the beam is achieved by coating a glass plate with several layers of alternating refractive index materials. In some cases, the reflected intensity can reach values near 99%. Although our technique does not encourage reflections, it is possible that SWT characteristics are inherent into our technique. This may fully explain the unexpected results.

There are two primary differences between the standing wave trap and our technique. First, SWT uses a beam that is usually not focused as tightly as that found in a gradient trap. In fact, the beam is more characteristic of a two-dimensional or radiation pressure trap as described previously. Second, the glass surface in SWT is coated with reflective layers to encourage the formation of a standing wave. While the techniques are not precisely the same, we might infer some general similarities between the two since the arrangements are nearly the same (focused trapping beam normally incident at a glass–water interface). For this reason, we would expect to see some reflection of the gradient trapping beam, especially as the focal point nears the plate surface, but the reflected amount is typically expected to be about 0.4% for an unmodified glass–water interface. In that case, we would not expect reflection to be an important consideration for our technique, but there is compelling experimental evidence that suggests otherwise.

4.3.2 Experimental Evidence of a Standing Wave

Examining the data for which there are obvious artifacts ("bumps" or discontinuities seen in plots of the mean intensity versus trap position—as shown in Figure 4-6), we see that these features appear at periodic intervals of about 400 nm. This corresponds well with the expected interval of $\lambda/2$ for a standing wave trap. Further evidence of this effect is provided by the individual position histograms where these intensity discontinuities occur. The appearance of two distinct potential energy minima is shown in Figure 4-7 for three slightly different locations of the trap center (offset by ~20 nm).
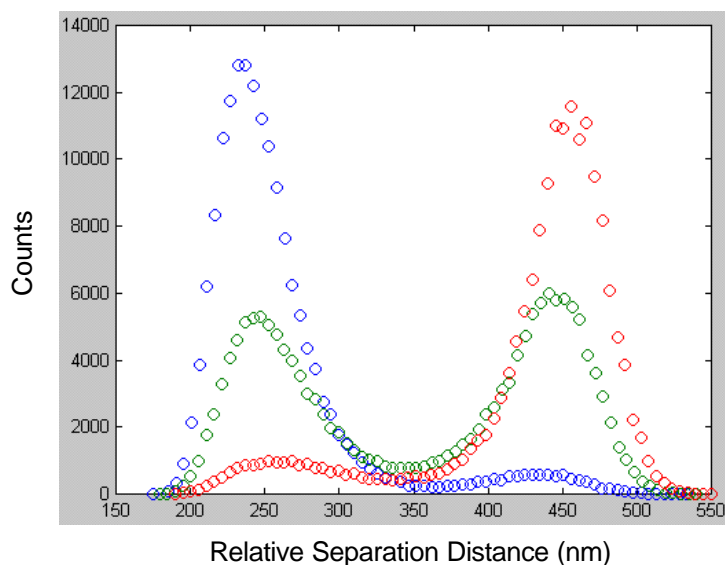
Figure 4-7. Position histograms for three slightly different locations (separated by 20 nm) of the trap center in a standing wave arrangement (1.0 *m*m silica).

For critical locations of the trap center, it is possible to create two local energy minima (corresponding to intensity maxima) of equal depth such that the particle will spend an equal amount of time in each. This result is possible if we consider an unusually deep secondary energy minimum, but this is expected from DLVO theory for the particle systems considered here. In addition, the effect occurs at regular intervals, lessening as the separation distance increases, which DLVO theory could never predict. The experimental evidence seems to support the generation of a standing wave as the cause of the unusual data.

To definitively prove the importance of reflections at the interface, the trajectory of a trapped particle was observed as the trap focus was stepped toward slide surfaces having reflective dielectric coatings. If experiments using uncoated glass slides show evidence of a standing wave, then a more reflective slide should show an exaggerated

effect. Several experiments were run to deduce the effect of a reflective surface.

Zemánek and co-workers supplied us with reflective glass slides using multiple layers of

dielectric materials (SiO_2 and TiO_2). We were provided two sets of coated slides having

1% and 25% reflectivity values (R). Experiments were performed using the standard

measurement procedures detailed previously. The trap center was moved in increments

of 40 nm toward the slide surface. A plot of the mean intensity data using these reflective

slides is shown in Figure 4-8.
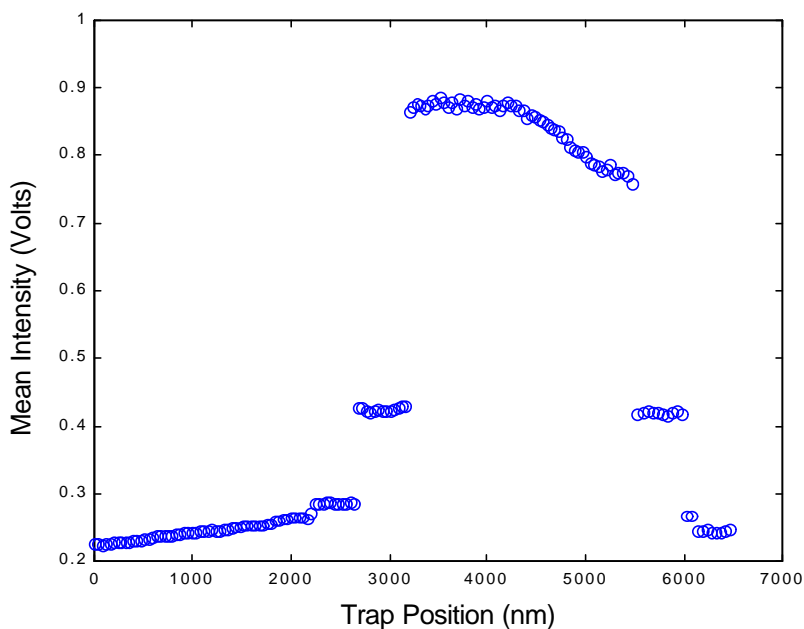
Figure 4-8. Mean intensity as a function of trap position for a 1.5 mm silica particle near
a reflective glass slide (R=25%).

The data show obvious discrete jumps of the particle from one stable trapping position to

the next as the trap focus is moved toward the slide. Notice also that as the focal point

moves beyond the interface, the particle actually moves away from the surface to a

location near its initial position. This is because there is sufficient reflection of the beam

to create a focus that moves away form the surface. The basic features of this data

demonstrate the clear existence of a standing wave since the particle essentially can only

find discrete positions with respect to the surface. Notice that this plot is an exaggeration

of the trends seen in Figure 4-6. The spacing of these discrete movements is found by

converting the intensity data in Figure 4-8 to position data, shown in Figure 4-9.

Figure 4-9. Mean relative separation distance as a function of trap position for a 1.5 *m*m
silica particle near a reflective glass slide (R=25%).

The three stable locations closest to the surface appear to be spaced nearly equally (~300

nm); this interval is consistent with the distance of $1/2$ seen in SWT (recall that the

wavelength of the trapping light in water is roughly 624 nm, since the frequency is

unchanged as it propagates through a dielectric material). In this arrangement, rather

than follow a single beam focus that moves in 40 nm increments, the particle is finding

the antinode with the highest intensity. Since the locations of the antinodes remain fixed

regardless of the location of the theoretical focal point, the particle is restricted to make

discrete movements from one antinode to the next as the intensity distribution shifts.

The variance of separation distance also shows interesting behavior as the particle

makes its discrete movements. This data is shown in Figure 4-10.
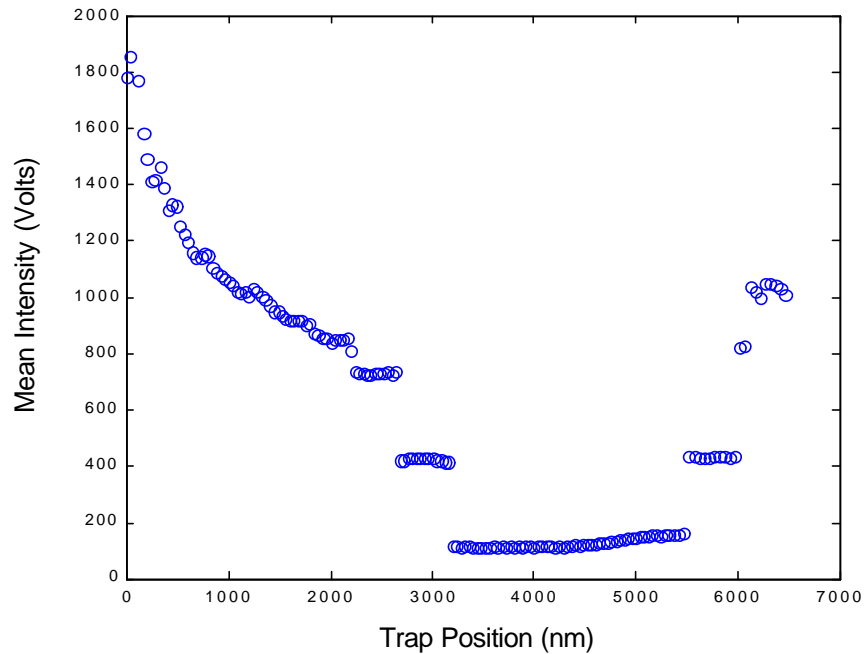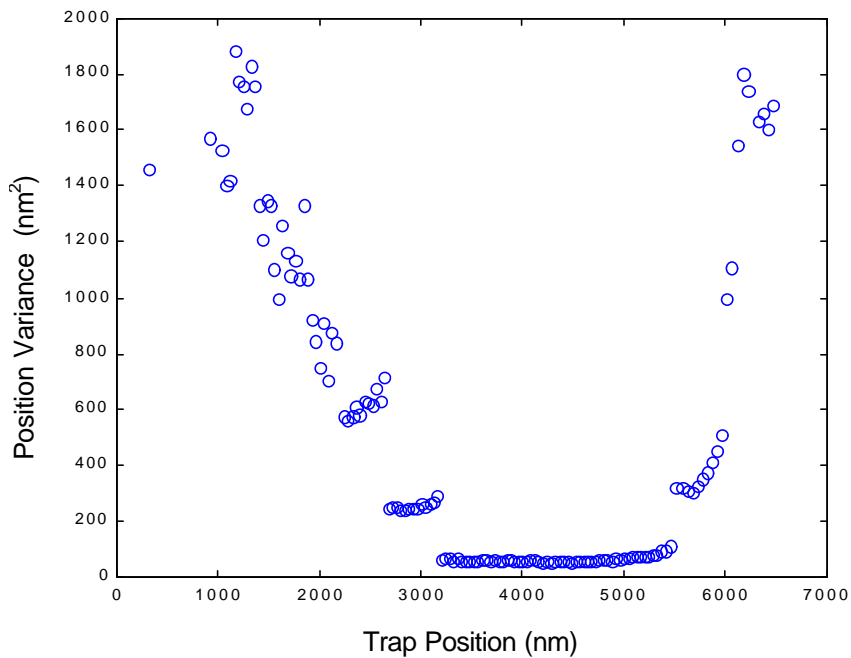

Figure 4-10. Variance of separation distance as a function of trap position for a 1.5 mm silica particle near a reflective glass slide (R=25%).

The variance of particle fluctuations decreases markedly as the particle approaches the surface. This indicates that the effective energy wells trapping the particles become increasingly sharp at shorter separations. This is expected since the interference of trapping light would be maximized when the focal point is very near the interface. Because the trap stiffness is inversely proportional to the position variance, the data are re-expressed as stiffness values in Figure 4-11.

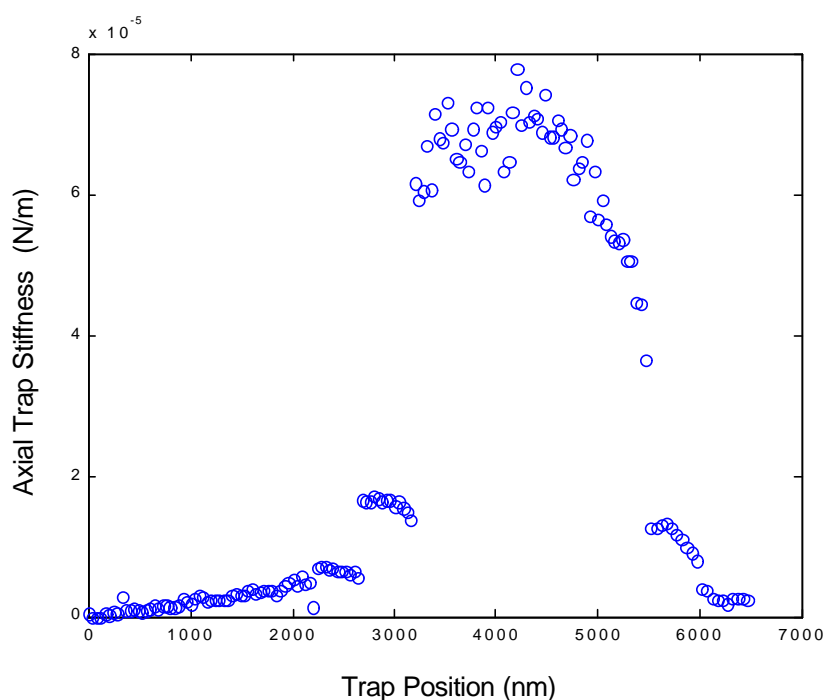Figure 4-11. Axial trap stiffness as a function of trap position for a 1.5 *m*m silica particle near a reflective glass slide (R=25%).

The trap stiffness gives a measure of the steepness of the potential well that holds the particle at any given antinode. This plot reiterates that the steepest well is located near the surface. The variability in the data is due to the sensitivity of the calculation upon the

measured variance since the stiffness grows quickly for small values of the variance. The magnitude of the trap stiffness seen in these measurements far exceeds the typical values observed for a usual force measurement experiment. Typical force measurements with micron-sized silica using the LaserTweezers 100 optical trap have consistently shown stiffness values ranging from 1×10^{-6} to 3×10^{-6} N/m (1 to 3 fN/nm). Figure 4-11 shows a maximum stiffness value that is at least an order of magnitude larger than what is typical for our technique. This maximum value may be elevated due to the presence of the particle–surface interactions, but even locations far from the plate show large stiffness values. These higher stiffness values are a novel aspect of SWT especially considering that a strong axial force can be created without requiring a high numerical aperture lens (i.e., a tight beam focus) or a large increase in laser power.

Similar results were obtained for studies using coated slides where R=1%, where the standing wave effects were less pronounced. The effects were greater than those seen for an uncoated glass slide, however. It is surprising that such a low reflectivity (R<1%) slide could give rise to these effects, but clearly the technique is highly sensitive to any such reflections. In fact, we ran additional experiments using an "anti-reflective" slide (R<0.15%) and saw no major improvements over measurements made with uncoated slides. The reason for this is likely that the reflectivity of the trapping beam is a strong function of incident angle. The predicted reflectivity values for these coatings assume at most a 30º deviation from normal incidence. The microscope objective lens (1.3 NA) used in these experiments, however, has a maximum convergent angle that is far in excess of this limit, so it may be that the actual reflectivity is much higher than the predicted value.

4.3.3 Modeling the Trapping Beam Profile Near a Reflective Surface

It is possible to predict standing wave behavior theoretically by using beam optics to describe the intensity profile near the glass–water interface. This is the subject of a publication by Zemánek et al. [39] where the force–distance profile of a Rayleigh sphere ($a \ll 1$) is predicted using a paraxial (PA) approximation of the light rays. In the case of a tightly focused beam, however, the PA assumption becomes quite poor. For highly convergent rays, higher-order corrections are required to accurately describe the EM fields of a Gaussian beam near the focal point. To our knowledge, no previous work exists that provides a theoretical description of a standing wave using a tightly focused beam (i.e., single-beam gradient trap).

CHAPTER 5
STATIC AND DYNAMIC FORCE MEASUREMENTS USING A REVISED
METHODOLOGY

5.1 Description of the Revised Methodology

Chapter 4 discussed the problems associated with reflection of the trapping beam

as its focus approaches the flat surface. Significant reflection of the beam can generate a

standing wave that compromises the accuracy of the technique. Rather than trapping the

particle into a single beam focal point, the actual electromagnetic field distribution may

be far more complex and lead to unexpected movements of the particle as the trap focus

is moved toward the flat surface. Though this is a problem when the trapping beam is

centered below the objective, the standing wave effects can be largely eliminated if the

beam is positioned to enter the objective slightly off-axis. We can adjust beam entry

point by sliding the trapping unit along the guide rail. A beam that is concentric with the

objective aperture gives the greatest standing wave effects and is considered undesirable

in force measurements. However, if the trapping unit is moved a small distance (a few

millimeters) in either direction from this location, the beam axis is incident at the slide

surface at a slight angle. This reduces the amount of retro-reflected light that can

interfere with the incoming beam.

The ideal position of the beam to reduce standing wave effects appears to depend

upon several factors related to the sample. The particle type and the precise placement of

the glass slide upon the microscope stage may both influence this ideal position. For the

results shown in this chapter, we adopted a trial-and-error approach to minimizing the

reflections. This is done by trapping a particle, positioning the trapping unit at some off-axis position, and then taking rapid samples of the intensity as a function of the trap focus position. If there is a significant standing wave effect, it is manifests as discontinuities in the statistics of the measured intensity. The trapping unit can then be repositioned and the diagnostic sampling repeated until an optimum location is found. In general, this optimum location will vary only slightly depending on the sample such that the trapping unit can be left in place to achieve satisfactory results. With this additional parameter optimized, the experiments proceed exactly as described in Chapter 3. As will be shown, data generated using this revised methodology are far superior to earlier measurement results where the trapping unit position was unaltered.

5.2 Static Force Measurements

5.2.1 Procedure Details

The measurements reported in this section precisely follow the experimental procedure described previously in Chapter 3. The specifics of this procedure are noted here. Two solutions of NaCl (0.23 and 1.0 mM) were prepared using Barnstead Nanopure ultrafiltered water. Silica microspheres of 1.0 and 1.5 μm nominal diameter ($\pm$ 0.1 μm) were purchased from Geltech as dry powers and suspended in the NaCl solutions at low particle densities ($\sim 10^5$ particles/mL) for a total of four different samples. A similar density of 9.14 μm diameter polystyrene spacer particles (Polysciences) served as gap spacers. Solutions were prepared the day of the experiment to eliminate contamination of the samples. The samples were sonicated to break up aggregates and mixed just prior to an experiment to resuspend the particles in solution. The He–Ne laser beam was a set to an incident angle of 63.7°. This gives an evanescent wave penetration

depth, b^{-1}, of 184.4 nm. The data acquisition program was set to acquire 65536

intensity samples at a sampling rate of 20 kHz for each trap position. The trap was

moved by 20 nm increments until the particle was found to achieve its minimum

accessible separation distance. The data was continuously saved to a file and analyzed at

a later time using the MATLAB analysis program.

5.2.2 Static Force Results

Figure 5-1 shows histograms of particle positions for a 1.5 mm silica sphere at

equilibrium separation distances of 56.2 and 543.7 nm, which correspond to regions

where the surface forces are appreciable and negligible, respectively.
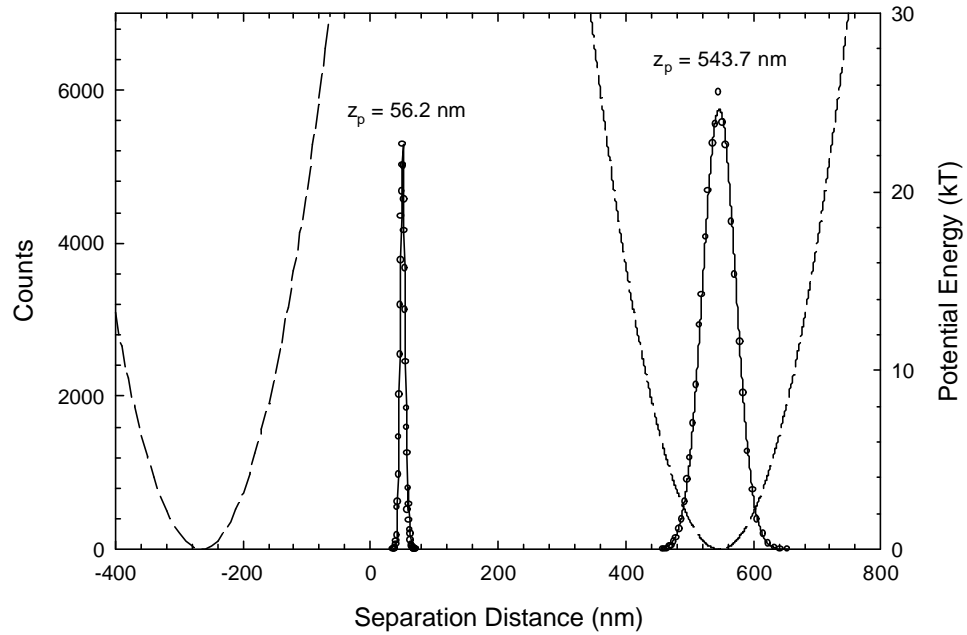
Figure 5-1. Measured histograms of particle positions and estimated potential energy
profiles corresponding to most probable separation distances of 543.7 and 56.2 nm.

The dashed lines are the predicted potential energy profiles in the absence of surface forces, equivalent to $f_{trap}(z)$. Note that it is possible to have a trap potential minimum theoretically located within the solid plate. The static force is calculated directly from the distance between the hypothetical trap minimum and the actual minimum. At $z_p = 543.7$ nm, the histogram is centered over the trap potential profile indicating a negligible static force. However, at $z_p = 56.2$ nm, there is a large deviation between the trap potential minimum and the most probable separation distance. Assuming that the trap potential is harmonic, the static force is simply proportional to the observed distance deviation as in equation (2.37).

Figures 5-2 and 5-3 show experimental force–distance profiles obtained for 1.0 and 1.5 μm silica spheres, respectively, interacting with a flat glass plate in 0.23 and 1.0 mM NaCl solutions.
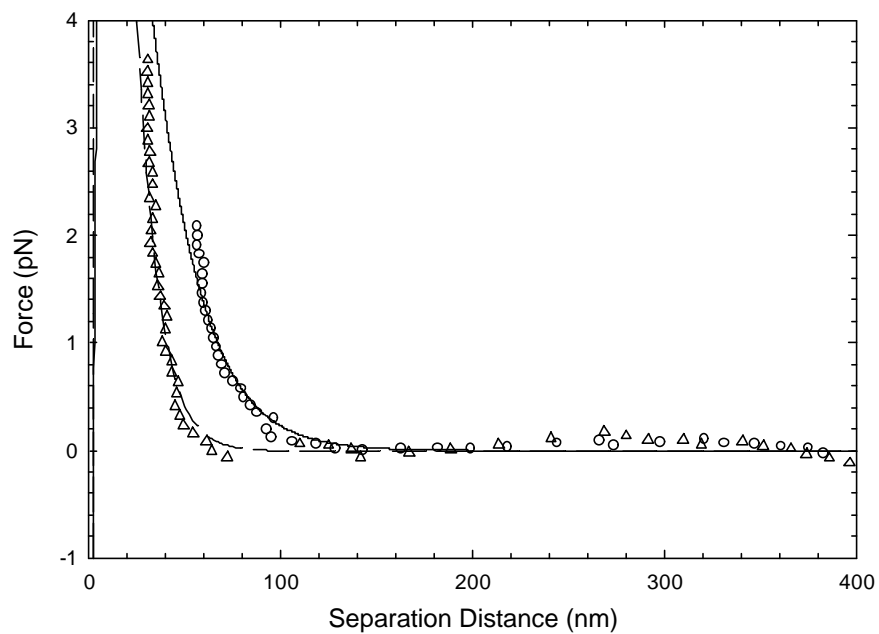
Figure 5-2. Static force measurements for a 1.0 **𝒏**m diameter silica sphere near a glass plate in 0.23 mM (○) and 1.0 mM (△) NaCl. DLVO theory predictions are plotted for both ionic strengths (0.23 mM – solid line, 1.0 mM – dashed line).
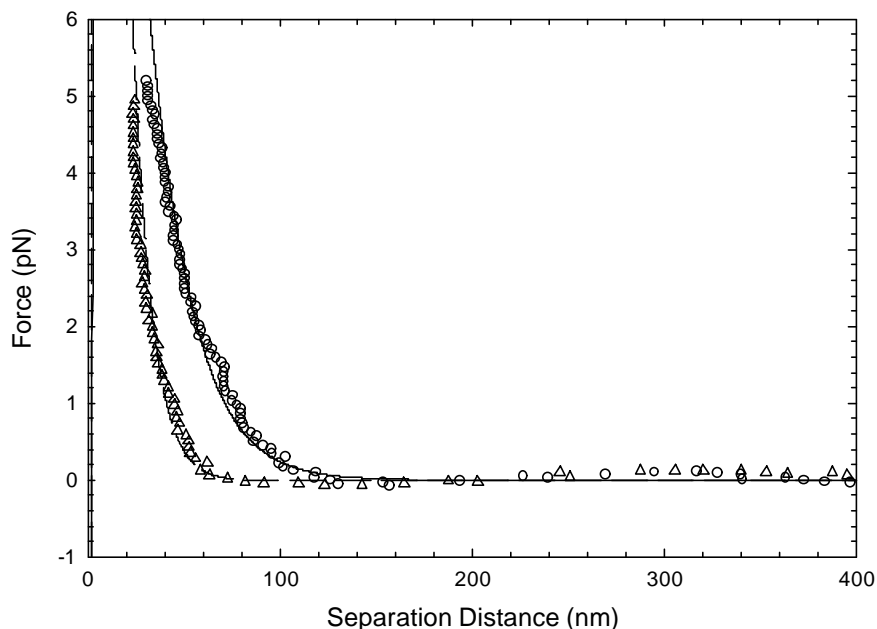
Figure 5-3. Static force measurements for a 1.5 μm diameter silica sphere near a glass plate in 0.23 mM ($\bigcirc$) and 1.0 mM ($\triangle$) NaCl. DLVO theory predictions are plotted for both ionic strengths (0.23 mM – solid line, 1.0 mM – dashed line).

The absolute separation distances were obtained by fitting the viscous drag coefficient data to equation (3.7), as discussed previously and shown below. From conductivity measurements, we were able to confirm the ionic strengths and accurately estimate the Debye lengths, k^{-1}, which represent the characteristic exponential decay of the double layer forces as a function of separation distance (k^{-1} = 20.0 nm for 0.23 mM NaCl, and k^{-1} = 9.6 nm for 1.0 mM NaCl). In each case we found very good agreement with DLVO theory (shown as solid and dashed lines in the static force plots), accounting for the combined effects of double layer and van der Waals interactions. The double layer force model is based upon the Debye–Hückel approximation, which assumes low surface potentials (absolute value of ~25 mV or less) and slightly overlapping double layers

(principle of superposition). Derjaguin's approximation is used to account for the curvature of the silica particle. The van der Waals model is based on Hamaker theory and neglects retardation and screening effects. The van der Waals force should be small enough in this range of separation distances such that a more accurate model is not required.

5.2.3 Discussion of Static Force Results

For the systems tested in this study, the dominant static force is generated by an overlap of the diffuse double layers where the repulsive force is sufficient to keep the particle from finding regions very near the surface where van der Waals attractive forces become appreciable. The double layer repulsive force, then, provides a convenient test of the accuracy of our technique since the agreement with theory does not strictly depend on the absolute separation distance. The DLVO theory profile was generated using literature parameter values and an experimentally derived value for the particle radius. By assuming shear plane potentials of –15 mV, the DLVO theory profile agreed well with our static force measurements. This value of the potential provided good agreement for initial experiments and was therefore used throughout as a fixed parameter. Although the actual shear plane potentials were not be verified independently for the silica particles and the glass slide directly, a shear plane potential of –15 mV is reasonable for SiO_2 at neutral pH conditions.

The static force results demonstrate the ability of the optical trap to apply a linear force to the particle for relatively large displacements from the trap center. Since the intensity profile of the focused trapping beam decays more gradually in the axial direction, the linear force regime can extend well beyond a particle radius. For the experiments reported here, we observed a linear response up to about one particle

diameter for a 1.5 mm diameter sphere. The linear force approximation was assumed to

be valid for regions where the static force profile agreed well with DLVO theory.

Measured forces clearly beyond the linear regime were omitted.

These revised measurements, which optimize the off-axis position of the trapping

beam, are greatly improved over the initial results shown in Chapter 4. The standing

wave effects are almost completely eliminated using this new methodology. However,

some slight effects remain no matter how carefully the off-axis position is chosen. Upon

closer examination, the static force data in Figure 4-2 and 4-3 show non-zero force

measurements in regions where the double layer and van der Waals forces should be

negligible. Consistently, there are small positive forces (~0.2 pN) that appear for

separations of about 300 nm. Also, there are small negative forces that appear just

beyond 100 nm. This leads to a slight wavy appearance of the overall force–distance

profile, although the errors are minimal. While this is likely due to slight interference

effects, it does not seem to disrupt the force data where significant forces (>0.5 pN) are

measurable. Overall, the measurements agree very well with DLVO theory predictions

which validates the accuracy of the technique for these particle systems. Because the

behavior of trapped particle within this complex electromagnetic field depends on the

particle size and material, the results may be better or worse. At present, it is difficult to

predict which particle systems will behave well within this trap although it appears that

higher refractive index particles (e.g., polystyrene) suffer greater effects due to the

standing wave. In fact, it was this early observation that led us to study silica particles

rather than equivalently sized polystyrene microspheres.

5.3 Dynamic Force Measurements

The dynamic (or drag force) interactions were also measured in this study. The data analysis occurs simultaneous to the static force analysis using the same time-series data. This analysis does not require any additional modifications of the experiments since the inherent Brownian fluctuations of the trapped particle are sufficient to measure its drag coefficient.

5.3.1 Dynamic Force Results

Figure 5-4 shows a plot of the autocorrelation function of intensity fluctuations at two particle positions (the same separation distances shown in Figure 5-2).
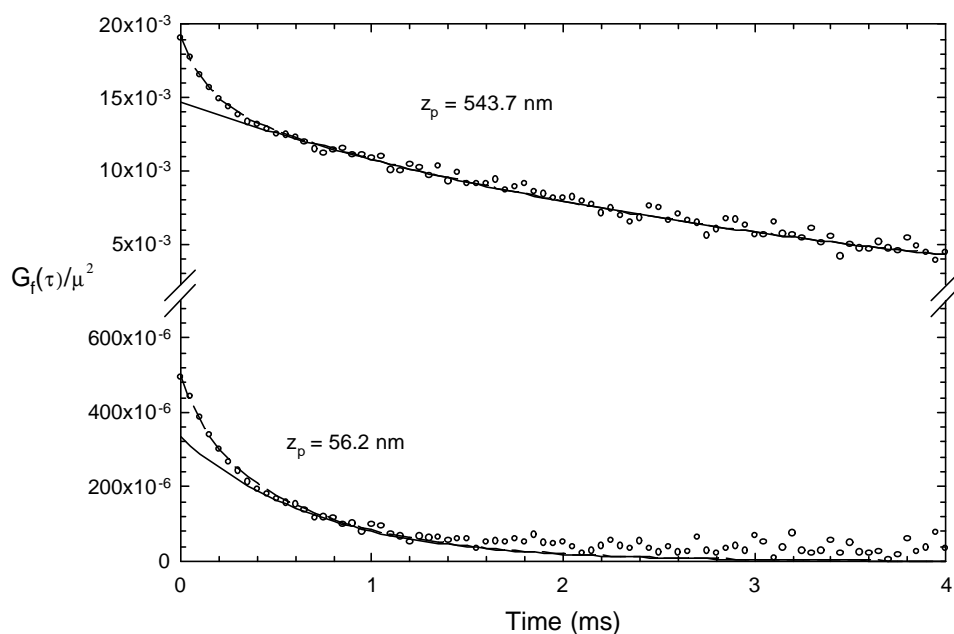
Figure 5-4. A plot of the intensity autocorrelation function ($\bigcirc$) at two separation distances for a 1.5 μm diameter silica sphere. The separation distances correspond to those shown in Figure 5-1.

The dashed line is a fitted curve corresponding to equation (3.16). These plots clearly

show the two characteristic decay times representative of the filtered noise and particle

motion. A fit at each trap position in the scan was used to estimate the relaxation time of

the particle fluctuations, from which the viscous drag coefficient was calculated.

Figures 5-5 and 5-6 show plots of the experimental drag coefficient data as a

function of separation distance. The solid and dashed lines represent the "exact" drag

coefficient profiles for the slow motion of a sphere normal to a flat wall [33].

Figure 5-5. Drag coefficient measurements for a 1.0 μm diameter silica sphere near a glass plate in 0.23 mM ($\bigcirc$) and 1.0 mM ($\triangle$) NaCl. Hydrodynamic theory predictions are plotted based on the fitted particle radius far from the surface (0.23 mM – solid line, 1.0 mM – dashed line).

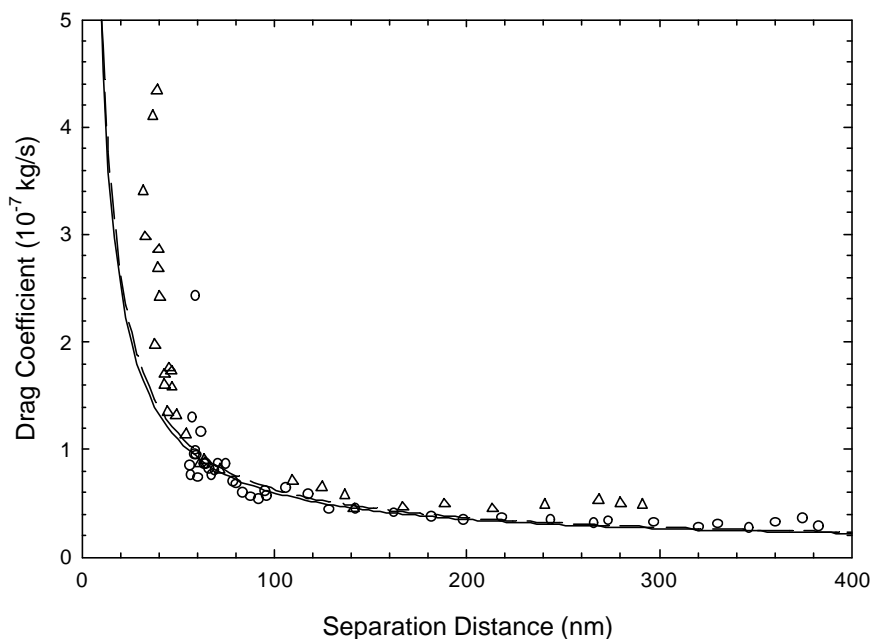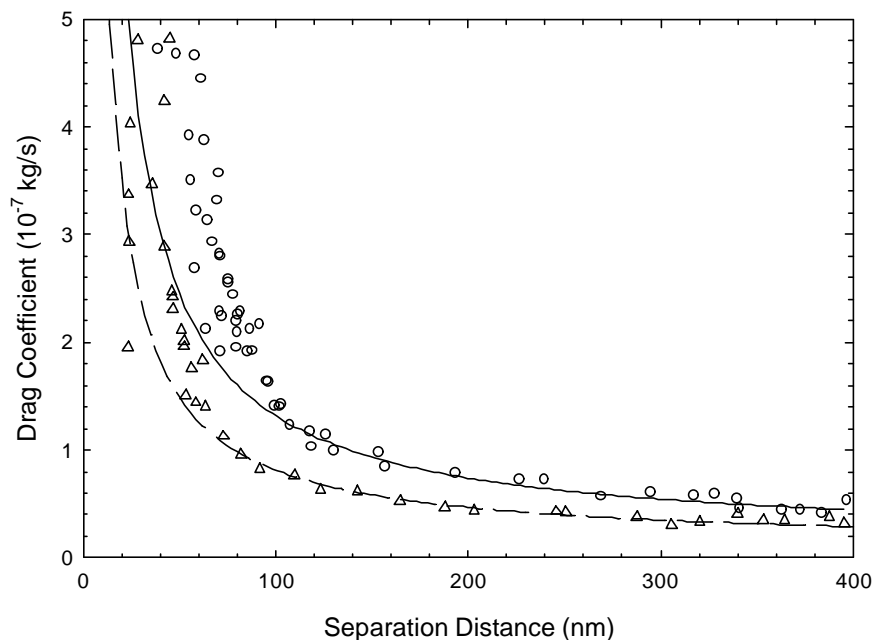Figure 5-6. Drag coefficient measurements for a 1.5 **m**m diameter silica sphere near a glass plate in 0.23 mM (○) and 1.0 mM (△) NaCl. Hydrodynamic theory predictions are plotted based on the fitted particle radius far from the surface (0.23 mM – solid line, 1.0 mM – dashed line).

These curves were fit to the data over the range where surface forces were negligible, using an offset distance as the only free fitting parameter. This fit provided the absolute distances for both static and dynamic force measurements. We observed excellent agreement with the theoretical hydrodynamic result when the double layers had minimal interaction with each other. However, as the double layers begin to overlap significantly the drag coefficient increases dramatically, even more so than the hydrodynamic theory predicts. This observation suggests that there may be an additional drag contribution due to the presence of the double layer ions. It is possible that electroviscous phenomena (due to the coupling of electrostatic and hydrodynamic interactions) can account for the higher than expected drag measurements [37, 38].

5.3.2 Discussion of Dynamic Force Results

If the deviation between the measured drag coefficient and theory is due to electrical double layer interactions, then we expect the separation distance where the deviation occurs to scale with the Debye length, which is the characteristic thickness of the double layer. This deviation occurred consistently at separations equal to about five Debye lengths, as shown in Figure 5-7 where the departure of the measured drag coefficient from the theory is plotted versus separation distance normalized by the Debye length.
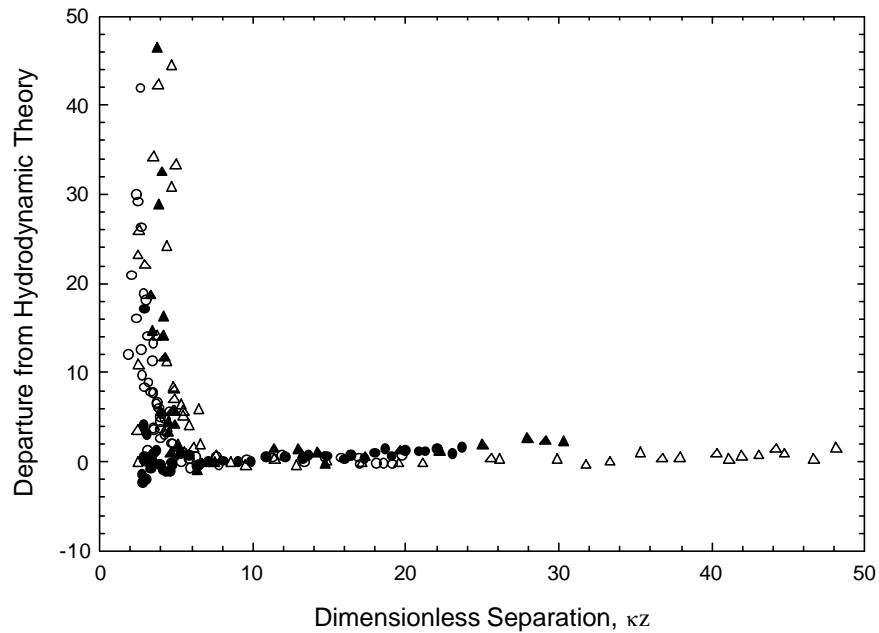

Figure 5-7. Dimensionless departure of the experimental drag coefficient from hydrodynamic theory.

The departure value is defined as $[I(z_p) - I_{theor}(z_p)]$, where $I(z_p)$ is the measured correction factor to Stokes' law and $I_{theor}(z_p)$ is the theoretical correction factor. All four

curves tend to show little deviation from theory until there is a significant overlap of the double layers (occurring at about five Debye lengths), which supports the hypothesis that the double layer ions contribute to the enhanced drag force.

While there is evidence that double layer interactions may lead to an enhanced drag force on the diffusing particle, it is also possible that the measurements are not accurate analyzed in this region. It has been observed that the fitting procedure used to deduce the relaxation time of particle fluctuations is progressively less accurate as the separation distance decreases. There appear to be two reasons for this. First, as the particle is trapped at small separations, the particle's motion becomes constrained such that the variance of fluctuations is extremely small ($\sim$10 nm^2 or less). If the motion of the particle is this small, it is difficult for the detection system to resolve movement this amid the system noise (background noise and shot noise). This is seen in Figure 5-4 for the autocorrelation function where z_p = 56.2 nm. Here, the fast decay (150 $\boldsymbol{ms}$) represents the filtering of white noise and the slow decay is due to particle motion. However, note that the noise contributions dominate such that an accurate fit of the data is difficult. Second, notice that the autocorrelation function does not decay to zero as expected. Rather, there is a non-zero baseline that undoubtedly affects the quality fit, and ultimately, the estimate of the drag coefficient. It is possible that there is a slowly relaxing process in the system (with a time scale on the order of seconds) that is leading to this effect. It is therefore difficult to determine whether the drag coefficient data is indicative of a physical process experienced by the particle or a measurement artifact.

CHAPTER 6
SIMULATING AND MODELING EXPERIMENTS

6.1 Brownian Dynamics Simulations of Trapping Experiments

The drag coefficient is determined by measuring the experimental autocorrelation

function of particle position shown in equation (3.12). This equation assumes that the

potential energy around the equilibrium position is harmonic, and that the drag

coefficient at the equilibrium location, $d(z_p)$, is insensitive to the sampling of other

nearby locations within the trap. In order to assess the accuracy of these assumptions, we

chose to test our model using theoretical time-series data generated by one-dimensional

Brownian dynamic simulations. Using an appropriate iterative algorithm [41] to solve

the Langevin equation for the motion of the particle, several seconds of real-time data

were generated for a particular location of the trap center. Simulations were performed

on Sun Microsystems Ultra 10 workstations running MATLAB. As with experimental

data, the autocorrelation function was determined from the time-series data, and a non-

linear regression was performed to estimate the drag coefficient. The simulation was

repeated for various locations of the trap center until a sufficient profile could be

produced. In all cases, the observed drag coefficient from the exponential fit was

assumed to be the value at the equilibrium separation distance.

6.1.1 Simulation Procedure

The trajectory of the particle was calculated at each Brownian time step ($\Delta t = 10^{-4}$

seconds) using an appropriate equation of motion (consistent with the Fokker–Planck

equation):

$$z(t + \Delta t) = z(t) + \frac{\partial D}{\partial z} \Delta t + \frac{DF}{kT} \Delta t + \boldsymbol{x}(t) \tag{6.1}$$

where z is the position of the particle, D is the diffusion coefficient of the particle (recall

that $D = kT/\boldsymbol{d}$), F is the total conservative force on the particle, and $\boldsymbol{x}(t)$ is a random

displacement that has a Gaussian distribution with a zero mean and whose variance is

$2D\Delta t$. This equation of motion is based on a more general expression from Ermak and

McCammon [41] for the trajectories of many colloidal particles in a viscous fluid. The

initial location of the particle is chosen to be as close to the location of the total energy

minimum as possible. The diffusion coefficient is calculated using the analytical

correction to Stokes' law given in equation (2.27) and the Stokes–Einstein relation given

in equation (2.23). The total conservative force is the sum of the trapping force and the

DLVO forces. The simulation was run until the simulated time far exceeded the

characteristic relaxation time, $\boldsymbol{t}_c$, of the particle movements with in the energy well. The

time-series data were then written to a PC file, and the process was repeated for the next

trap center position. Upon completion of the simulation, the saved data was then

decimated (to simulate the process of sampling real-time data with the acquisition

system) and analyzed by finding the autocorrelation function of particle fluctuations and

fitting the result with equation (3.12) using nonlinear regression. With a value for the

relaxation time, the drag coefficient is simply $d = t_c kT / s_z^2$. This value is then recorded

as the drag coefficient measured at the most probable position, z_p. The results can then

be compared with the theoretical prediction from Brenner [33].

6.1.2 Simulation Results

The results of this simulation showed that the drag coefficient is accurately

predicted using the autocorrelation analysis. Figure 6-1 shows a comparison between a

Brownian dynamics simulation results and Brenner's hydrodynamic predictions.
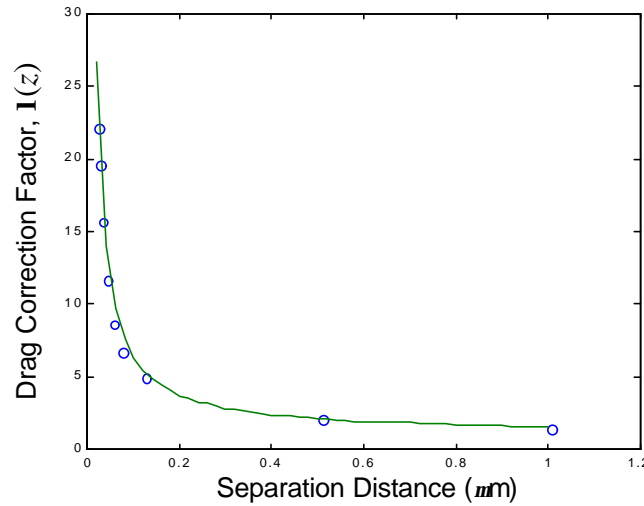
Figure 6-1. Simulated experimental drag ($\bigcirc$) versus Brenner's correction to Stokes' law.

Over the entire range of separation distances, we see excellent agreement between

simulations and Brenner's result. The simulations will not reveal anything new about the

hydrodynamics since the algorithm implements Brenner's analytical result, however the

simulation can tell us how accurate equation (3.12) is for extracting dynamic information

from time-series data. In the case of ideal data acquisition (i.e., noiseless, unfiltered), the

simulation demonstrates that we should be able to construct a very accurate drag profile

for the trapped particle. It also turns out that an accurate measurement of the drag is

nearly insensitive to the sampling rate. That is, the low sampling rate alone cannot bias

the measured drag data sufficiently to account for deviations such as those seen in

Figures 5-5 and 5-6. We might suspect that the analog low-pass filter is the cause of the

deviations, but the relaxation time would not be expected to fall below the filter time

constant of 150 *ms*. As such, the current sampling method should provide accurate

measurement of the drag coefficient over the entire range of separation distances.

The simulated data can be further processed to approximate the effects seen in

actual measurements. For example, passing the data through a digital filter can

approximate the analog RC filter of the preamplifier. A simple iteration is used in the

time-domain to implement a first-order low-pass filter:

$$\bar{x}_i = a\bar{x}_{i-1} + (1-a)x_i \tag{6.2}$$

where $\bar{x}_i$ is the newly filtered data point, $\bar{x}_{i-1}$ is the previously filtered data point, and a

is the *degree of filtering*. The time constant of the filter, t_f, is related to the degree of

filtering in the following way:

$$a = \frac{t_f}{t_f + T_s} \tag{6.3}$$

where T_s is the sampling period (inverse sampling frequency). As an initial condition, $\bar{x}_0$ is usually defined to be equal to x_0. The analog and digital filter outputs do vary slightly in the amount phase lag experience. The measurements are not particularly sensitive to the phase shift induced by filtering, so this is of little importance. However, experiments that externally oscillate the particle could suffer greatly from this phase shift, so either type of filter could affect future experimental results.

Also of interest is the effect of white noise on the data analysis. By converting the simulated position data to intensity values using equation (2.30), random white noise can be added to the intensity data. The magnitude of the noise corruption is related to the variance of the noise distribution, and this parameter can be altered to investigate its effect upon drag measurements. Such simulations may offer further insight into the nature of the enhanced drag measurements reported in Chapter 5. It is possible that the noise in the system far exceeds the measurable variance due only to particle motion, thus leading to a poor estimate of the drag coefficient for these regions of double layer overlap.

6.2 Modeling Statistical Data Generated from Force Measurements

A convenient way to quickly assess an experiment is to examine the statistics of the intensity measurements. The mean and variance profiles of the intensity as a function of trap position have distinctive shapes that are system specific (e.g., evanescent wave penetration depth, Debye length, background scattering, etc.). For example, the shape of these profiles will change if we alter the ionic strength of the solution. We can accurately model these profiles using experimental parameters and estimates of the interaction energy from DLVO theory. This is useful during an experimental run where the mean

and variance profiles are used as a diagnostic tool to assess its accuracy. If there is a problem with the run at some point (e.g., a second particle becomes trapped), these profiles will show uncharacteristic behavior that can readily be identified.

Prior to modeling these profiles, it was not always known whether a particular data set contained accurate data until after a full analysis was made to produce force data. Because of the time associated with analyzing the data, it is desirable to only analyze data sets that are likely to produce accurate force measurements. To this end, we have developed a strategy for estimating the mean and variance of scattered intensity as a function of trap position. The procedure is relatively simple and attractive in that it does not require a full Brownian dynamics simulation to produce these statistics. However, it tells us nothing about the hydrodynamics of the particle.

6.2.1 Modeling Procedure

The general procedure for modeling these profiles is given below:

1. Starting at a relatively large separation distance (~1000 nm), calculate the theoretical total potential energy of the particle (sum of harmonic trap potential energy and DLVO energy). Find the minimum potential energy and subtract this value off. This yields energies relative to the minimum and is important to ensure numerical stability for the calculation in Step 2.

2. Using Boltzmann's law, calculate the equilibrium probability distribution for the trapped particle. This distribution is in terms of separation distance.

3. Create an equivalent probability distribution for intensities by using equation (2.30).

4.   Calculate the mean and variance of the resulting intensity distribution:

$$\langle I \rangle = \sum p(I)I\Delta I \Big/ \sum p(I)\Delta I$$

$$s_I^2 = \sum p(I)I^2\Delta I \Big/ \sum p(I)\Delta I - \langle I \rangle^2$$

5.   Record the values for this position and move the location of the trap center a

        small distance (10 to 100 nm) closer to the surface. Return to Step 1.

6.   After many iterations of Steps 1 to 5, plot both statistical quantities versus the

        trap position. These results should resemble accurate experimentally derived

        statistics of the scattered intensity.

<u>6.2.2 Modeling Results</u>

        This procedure was used to create a MATLAB program for calculating intensity

statistics. The predicted profiles can very closely resemble actual experimental results.

Figure 6-2 shows the mean intensity profile for a 1.5 mm silica particle in a 0.1 mM NaCl

solution compared directly with a model prediction for the same system.
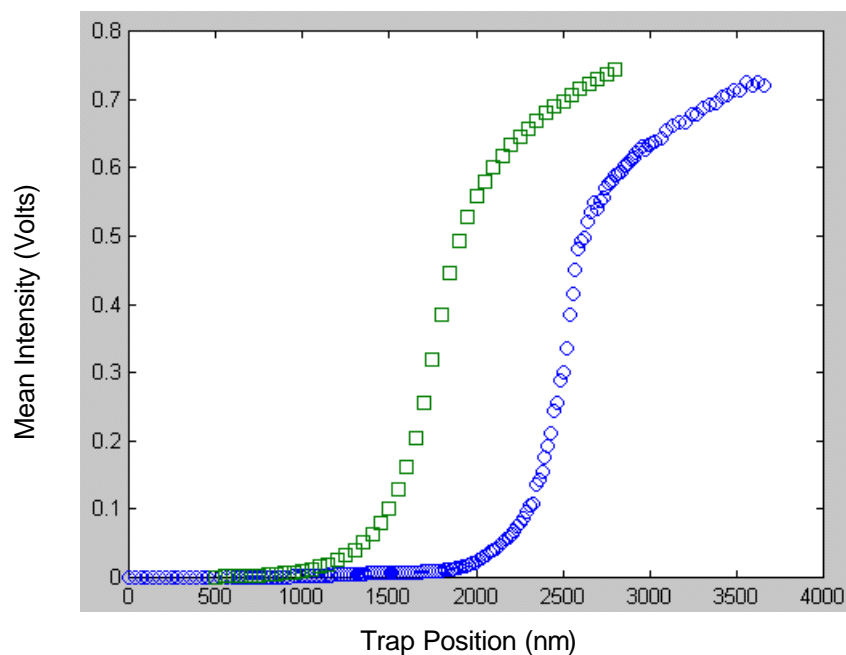
Figure 6-2. Model prediction (□) and experimental data (○) of the mean intensity profile.

The profiles are intentionally offset by 1000 nm for clarity. In this case, the profiles are

surprisingly similar in shape which indicates that the measurements were mostly likely

successful. There are some slight irregularities in the experimental data around the

inflection point (intensities between 0.15 and 0.5 V), but this is to be expected due to

slight interference effects that are unavoidable. Agreement is also seen with the variance

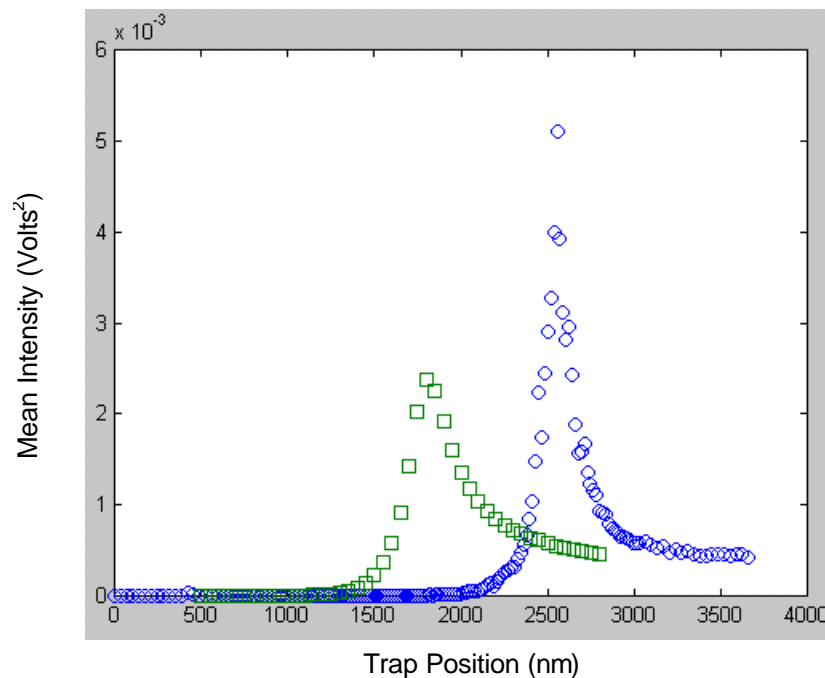profile shown in Figure 6-3 for the same system.

Figure 6-3. Model prediction (□) and experimental data (○) of the intensity variance profile.

In this comparison, the model appears to underpredict the variance slightly. This is expected, however, because of noise contributions that increase the variance. It also appears that the shape of the profiles not precisely the same. In particular, the width of the peak predicted by the model appears to be slightly larger than the experimental data. It is likely that standing wave effects, although slight, may contribute to some deviations. This would be more evident in the variance profile as opposed to the mean profile; this appears to be the case here.

While it gives quantitative results, the model is probably most useful for demonstrating the qualitative trends one should expect during a particular experiment. This allows the user to quickly identify whether the measurements are producing accurate

results or if there is a problem. Often, these problems can be diagnosed and fixed due to

an understanding of the expected trends. Because the model incorporates DLVO theory,

it can also identify which runs are best suited for further analysis.

CHAPTER 7
CONCLUSIONS AND SUGGESTIONS FOR FUTURE WORK

7.1 Static Force Measurements

We have shown that our technique can accurately measure static forces that arise between a micron-sized spherical particle and a flat surface. Excellent agreement was observed between measurements and DLVO theory using micron-sized silica particles in solutions of varying ionic strength. Initial force measurements did show anomalous results that suggested the possibility of strong attractive forces near the surface, but this was later shown to be due to standing wave effects. Experiments using reflective slides showed that the retro-reflection of the trapping beam could cause significant interference of the electromagnetic fields which can lead to inaccurate results, even for a glass–water interface. We were able to improve the measurement accuracy significantly by positioning the beam slightly off-axis with respect to the rear aperture of the objective. This reduced the amount of reflected light that contributed to the interference effects. Though the accuracy of the measurements was greatly improved, the standing wave effect could not be completely eliminated using this method. Depending on the type of particle used (e.g., size, refractive index), the standing wave effect may be more or less pronounced. In some cases, it may be impossible to eliminate the effect sufficiently to give accurate results. This is because the trapping force developed on the particle is a strong function of the exact electromagnetic field distribution and the dielectric properties of the particle.

7.2 Dynamic Force Measurements

The technique is able to measure the drag force on the particle as a function of its position for the flat surface. We accomplish this by calculating the intensity autocorrelation function and fitting this to a model predicted from the Fokker–Planck equation. A nonlinear regression fit of the data yields the relaxation time of particle fluctuations within the trap and ultimately leads to a calculation of the drag coefficient at the most probable position. The drag data were compared to Brenner's analytical correction for the slow motion of a sphere normal to a solid wall. We observed good agreement for separations where there was little overlap of the double layers. However, closer to the surface, the data showed enhanced drag that was underpredicted by hydrodynamic theory. Because the deviation was found to occur consistently at about five Debye lengths, it is possible that the electrostatic and hydrodynamic interactions are coupled to increase the drag force on the particle. However, we also observed that the regression fit in this region becomes somewhat poor because of a low signal-to-noise ratio, and because the autocorrelation function does not decay to zero as expected. Unless the noise level is reduced in this measurement region, it may be difficult to accurately estimate the drag coefficient.

7.3 Suggestions for Future Work

The new technique can now be used to measure more complicated systems including sub-microscopic particles, solutions of varying rheological properties, and spherically shaped microorganisms. There are also several key adaptations of the current technique that were in the process of implementation. The most notable recommendations are presented below.

7.3.1 Assembly of an Improved Optical Trap

A new optical trap has been designed for use with the current system and will ultimately replace the commercial LaserTweezers 100 unit. A schematic of the optical trapping system is shown in Figure 7-1.
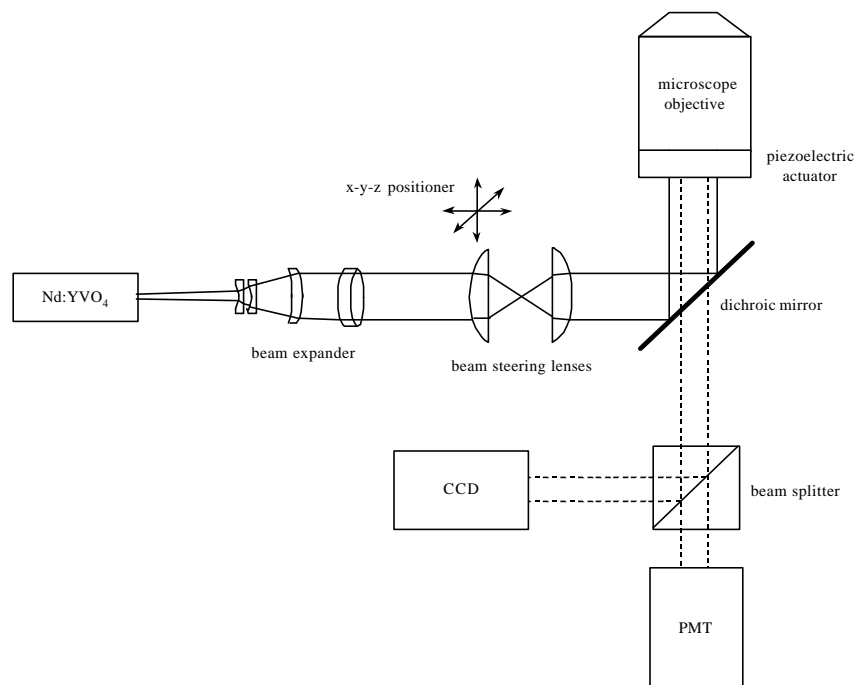
Figure 7-1. Schematic for a custom optical trapping system.

The new trapping system uses a 1.5 W Nd:YVO$_4$ solid state laser (l=1064 nm) with an adjustable power control, high precision optical components to minimize spherical aberration effects, a three-axis mounted aplanatic lens for steering the beam laterally and adjusting the parfocality of the laser spot, and a single-axis piezoelectric positioner for repeatable nanometer-scale movements of the trapped particle. The piezoelectric positioner is computer controlled and can be programmed to apply a variety of forcing

functions to dynamically move the trapped particle within the fluid. This is a significant improvement over the current focus control which uses a stepper motor. The stepper motor suffers from backlash effects when the direction of the motor is suddenly reversed which leads to significant hysteresis when positioning the trapped particle.

7.3.2 Reduce Noise in Measurements

The current system removes noise from the measurements by passing the signal through an analog RC circuit that acts as a low-pass filter. This eliminates most of the uncorrelated white noise from the signal before it is passed to the data acquisition system. However it is more desirable to reduce the noise contributions due to the electronic circuitry by cooling the photodetector. A new cooled PMT has been implemented for this purpose, but the results show that cooling alone has little effect on the overall noise in the system. The cooled photodetection system also has an analog filter, but with a very small time constant (7 $\boldsymbol{m}$) which passes nearly any frequency without removing much of the noise. Assuming that cooling the detector significantly reduces most of the electronic noise contributions, the other possible sources of noise are due to shot noise (from the discrete nature of photons striking the detector), and background sources. The background variance is almost always very small, so shot noise is the most important contribution to consider.

Added variance due to shot noise increases linearly with the mean of the scattered intensity. This proportionality constant is estimated by measuring the signal of a fully attached (non-fluctuating) particle. This allows the analysis program to correct the measured variance for shot noise effects by simply subtracting it away from the measured profile. In terms of the calibration procedure, this is an effective way of correcting the

estimate of the trap stiffness. However, when calculating the intensity autocorrelation function for dynamic measurements, the shot noise contributions cannot be subtracted in this manner. The ratio of the shot noise variance to the mean intensity is *constant* with mean intensity (as described above), but the ratio of the variance due solely to particle movements to the mean intensity *decreases* as the intensity increases. This means that shot noise contributions may begin to dominate as the particle is trapped very close to the surface (since the energy well in this region is very steep and the particle fluctuations correspondingly small). Here, the measured intensity time-series has a mean value that is associated with the particle's average position from the flat plate, but the variance of this signal is almost entirely due to shot noise. To get an accurate estimate of the relaxation time of the particle in the trap, we must be able to measure an appreciable variance due to the particle's motion. Unfortunately, if the shot noise dominates, it is difficult to fit the resulting autocorrelation function effectively. The drag measurements will continue to be inaccurate in this region unless a reasonable solution can be found.

7.3.3 Investigate Possible Electroviscous Effects

Assuming that a suitable strategy is found to remove most contributions of noise, the drag coefficient should be measured accurately for small separations where there is an appreciable double layer overlap. It is possible that an enhanced drag will be measured under these conditions due to a coupling of the electrostatic and hydrodynamic interactions. This is predicted theoretically, but it is not yet known if the effect will be significant for the particles used in these studies or if the measurement technique will be able to measure this for reasonable time scales.

7.3.4 Measure Specific Interactions of Bacteria with Coated Surfaces

Until now, we have only considered non-specific forces that vary as a function of separation distance. However, specific binding interactions (e.g., receptor–ligand) are important for bacterial adhesion and may be measurable using this technique. The protocol for these measurements is yet to be devised, but it will have to consider an interaction energy surface that accounts for both non-specific forces (along the separation distance axis) and specific binding forces (along an axis indicative of the number of bonds). The attachment of a bacterium will follow a trajectory along this energy surface until the cell is attached. The difficulty with these measurements is that the particle can fall into a primary minimum where the force is attractive and likely far in excess of the trapping strength. On approach to the surface, the bacterium will find a critical distance and jump into the primary minimum almost spontaneously. Thus, the force or energy profile will have to be mapped using a stochastic analysis that somehow measures the probability of attachment for a given set of conditions.

7.3.5 Force Measurements with Sub-Microscopic Particles

The technique is theoretically capable of measuring interactions for any sized particle as long as there is an appreciable scattered intensity emitted from the particle. As the particle diameter is reduced, the measured signal becomes weak, which may set a lower limit on the size that we can effectively use. Preliminary experiments using particles with diameters from 0.2 to 0.5 μm have shown promise using this technique. While the success of these experiments will greatly depend on the ability to reduce the noise, it appears that these measurements are entirely possible. Of particular interest in this size range are the interactions of viruses with flat surfaces. These would be the first such measurements of their kind and may provide insight on the attachment mechanisms

of viruses to surfaces. Also, as the particle radius decreases, Derjaguin's approximation
(the scheme for calculating interaction force or energy for curved surfaces) becomes
poor, and predictions using DLVO theory will no longer be accurate. Thus, direct
measurements using sub-microscopic particles will be of great benefit.

7.3.6 Measure Complex Properties of the Interface

Systems that have complex rheological characteristics near the solid–liquid
interface are of interest as well. For example, the presence of polymeric molecules near
the interface may give rise to viscoelastic behavior that can be monitored using this
technique. By applying a forced oscillatory motion to the particle via a moving trap
center, the rheological properties of the complex fluid can be probed directly. This
involves a revised analysis that accounts for the motion of the trap center and the
viscoelastic behavior of the fluid.

To consider dynamic trap movement and complex rheology, we introduce a
generalized Langevin equation:

$$m\frac{d^2 z}{dt^2} = -\boldsymbol{g}_z (z - z_0(t)) + H(t) + \boldsymbol{x}(t) \tag{7.1}$$

where $z_0(t)$ is the time-dependent position of the trap center, and $H(t)$ is a combined
force contribution from the complex fluid and the presence of surface forces, containing
both static and dynamic elements. By transforming equation (7.1) into the frequency
domain, we can find an expression for the power spectral density. Analysis of the
experimental power spectrum yields information about the nature of the fluid, and can be

decomposed into viscous and elastic contributions which may be a function of frequency as well.

The use of an oscillating trap may also be of interest for measurements where the inherent particle variance is extremely small. In these regions, the noise of the system can dominate the measured fluctuations due to the particle's movement and the measured drag coefficient can be in serious error. By inducing the particle to move with sufficient amplitude, the drag measurements can be improved significantly. This is one possible way of improving the drag measurements if other means of reducing the system noise fail.

APPENDIX
LABVIEW CODE FOR DATA ACQUISITION

A program was written in LabVIEW to automate the movement of the optical trap

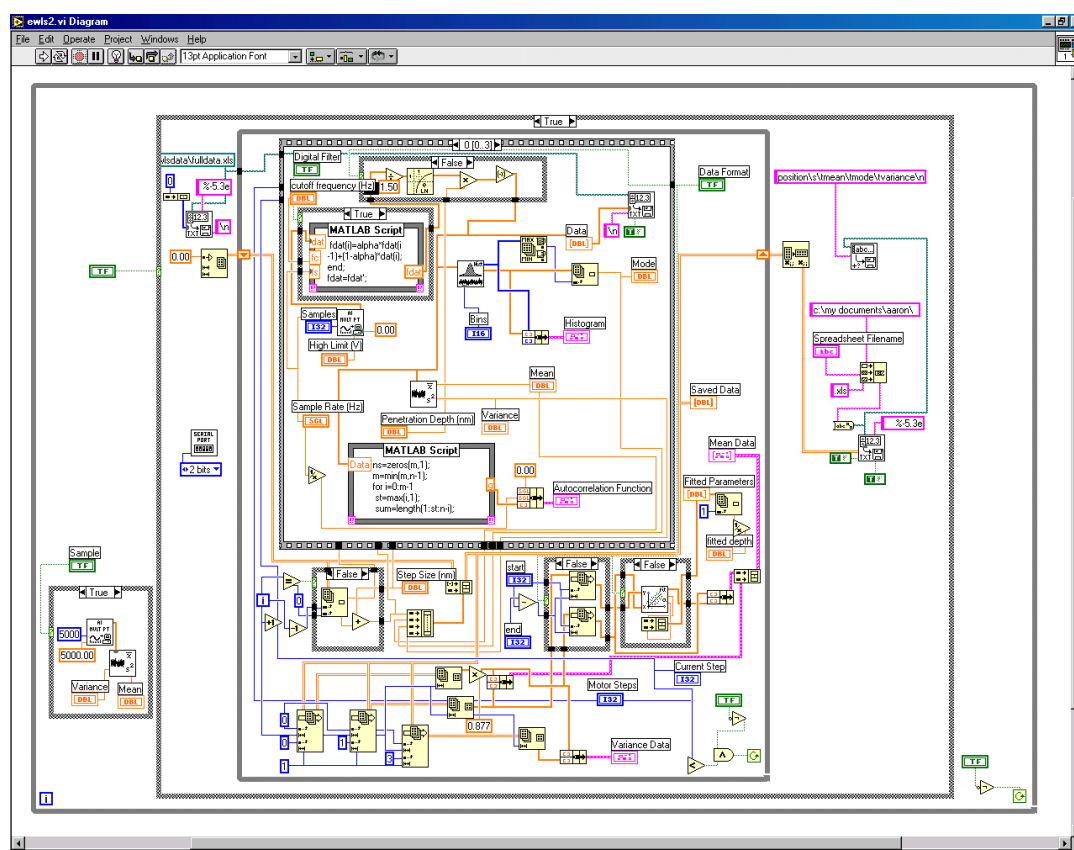focus and to collect the data. The wire diagram for this program is shown in Figure A-1.

Figure A-1. LabVIEW wire diagram for the data acquisition program.

The graphical programming language implements a wiring scheme to link subunits of the

program together. The graphical user interface of the program is shown in Figure A-2.
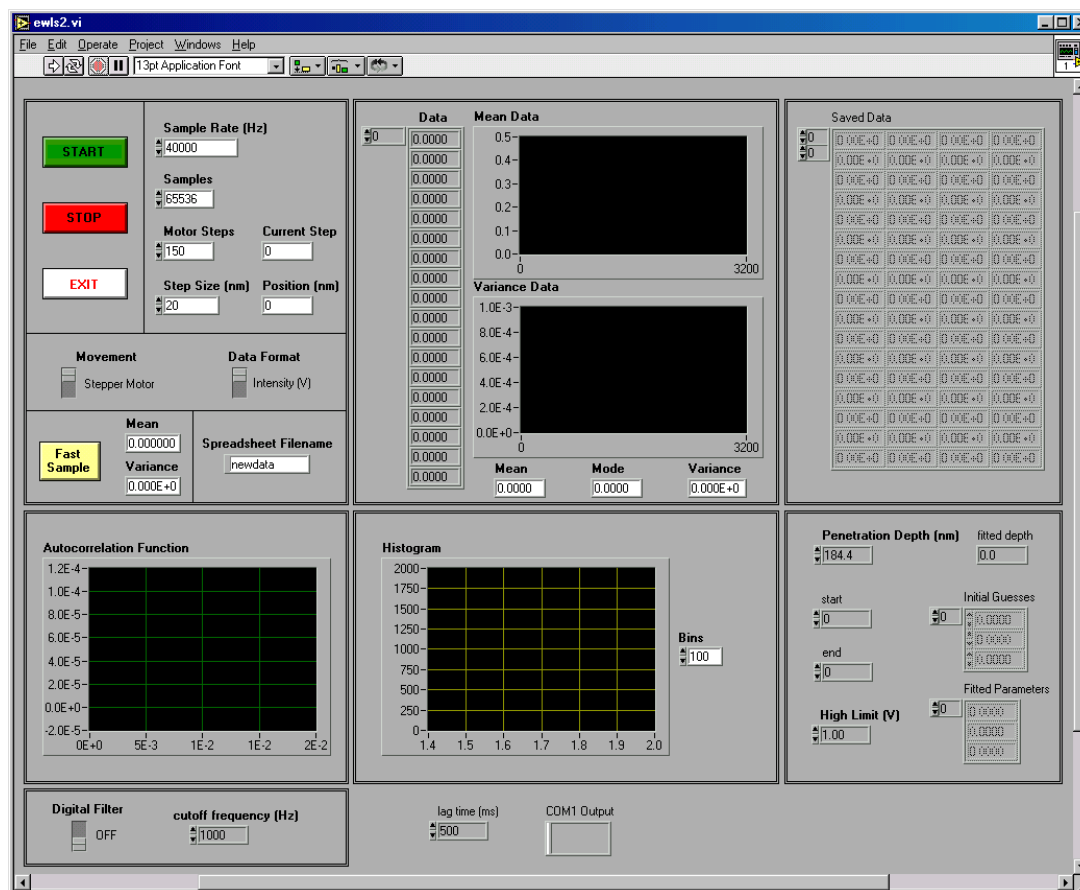
Figure A-2. LabVIEW panel display for the data acquisition program.

Once the program is started, the data acquisition procedure is fully automated until the

user instructs the program to stop. This is done either manually (by clicking the red

"STOP" button) or automatically by specifying the total number of steps. The data is

displayed in real-time as graphs and arrays of collected data. The program displays the

mean and variance of intensity measurements as a function of trap position in the topmost

windows. The autocorrelation function is shown in the lower left window. This is

calculated by sending the data to MATLAB and returning the results to LabVIEW. A

histogram of the data is shown in the lower middle window. These allow the user to

quickly evaluate the quality of the data as the experiment is progressing. There is also a

control option for using either a stepper motor or a piezoelectric device for moving the

location of the trap focus. Future versions of the program will likely produce force

information in real-time as the data is analyzed continuously after each trap step. This

would eliminate the need to save the raw data file which can exceed 100 MB in size

depending on the number of samples and steps.

LIST OF REFERENCES

1. Derjaguin, B.V., & Landau, L., Acta Physicochim. URSS 14, 633 (1941).

2. Verwey, E.J.W., & Overbeek, J.Th.G., "Theory of the Stability of Lyophobic Colloids" Elsevier: Amsterdam (1948).

3. Hermansson, M., Colloids Surf. B 14, 105 (1999).

4. Israelachvili, J.N., & Adams, G.E., J. Chem. Soc. Faraday Trans. I 74, 975 (1978).

5. Ducker, W.A., Senden, T.J., & Pashley, R.M., Nature (London) 353, 239 (1991).

6. Binnig, G., Quate, C.F., & Gerber, C., Phys. Rev. Lett. 56, 930 (1986).

7. Israelachvili, J.N., "Intermolecular and Surface Forces" Academic Press: San Diego (1992).

8. Prieve, D.C., Luo, F., & Lanni, F., Faraday Discuss. Chem. Soc. 83, 297 (1987).

9. Brown, M.A., Smith, A.L., & Staples, E.J., Langmuir 5, 1319 (1989).

10. Brown, M.A. & Staples, E.J., Langmuir 6, 1260 (1990).

11. Ashkin, A., Phys. Rev. Lett. 19, 283 (1970).

12. Ashkin, A., Dziedzic, J.M., Bjorkholm, J.E., & Chu, S., Opt. Lett. 11, 288 (1986).

13. Clapp, A.R., Ruta, A.G., & Dickinson, R.B., Rev. Sci. Instrum. 70, 2627 (1999).

14. Hiemenz, P.C. & Rajagopalan, R., "Principles of Colloid and Surface Chemistry" Marcel Dekker: New York (1997).

15. Garbassi, F., Morra, M., & Ochiello, E., "Polymer Surfaces from Physics to Technology" Wiley: Chichester (1994).

16. Stern, O., Z. Elektrochem 30, 508 (1924).

17. Derjaguin, B.V., Kolloid Z. 69, 155 (1934).

18. Hogg, R., Healy, T.W., & Fuestenau, D.W., Trans. Faraday Soc. 62, 1638 (1966).

19. Wiese, G.R., & Healy, T.W. Trans. Faraday Soc. 66, 490 (1970).

20. Ohshima, H., Healy, T.W., & White, L.R., J. Colloid Interface Sci. 90, 17 (1982).

21. Grant, M.L., & Saville, D.A., J. Colloid Interface Sci. 171, 35 (1995).

22. Sader, J.E., Carnie, S.L. & Chan, B.Y.C., J. Colloid Interface Sci. 171, 46 (1995).

23. Keesom, W.H., Physik A 22, 129 (1921).

24. Debye, P., Physik Z. 22, 302 (1921).

25. Hamaker, H.C., Physica IV, 1058 (1937).

26. Lifshitz, E.M., Sov. Phys. JETP 2, 73 (1956).

27. Gregory, J., J. Colloid Interface Sci. 83, 138 (1981).

28. Fowles, G.R., "Introduction to Modern Optics" Holt, Rinehart, and Winston: NewYork (1975).

29. Chew, H., Wang, D.S., & Kerker, M., Appl. Opt. 18, 2679 (1979).

30. Svoboda, K., & Block, S.M., Annu. Rev. Biophys. Biomol. Struct. 23, 247 (1994).

31. Tlusty, T., Meller, A., & Bar-Ziv, R., Phys. Rev. Lett. 81, 1738 (1998).

32. Helstrom, C.W., "Probability and Stochastic Processes for Engineers" Macmillan: New York (1984).

33. Brenner, H., Chem. Eng. Sci. 16, 242 (1961).

34. Derjaguin, B.V., Rabinovich, Y.I., & Churaev, N.V., Nature (London) 272, 313 (1978).

35. Velegol, D., Anderson, J.L., & Garoff, S., Langmuir 12, 675 (1996).

36. Velegol, D., Anderson, J.L., & Garoff, S. Langmuir 12, 4103 (1996).

37. Warszynski, P., & van de Ven, T.G.M., Adv. Colloid Interface Sci. 36, 33 (1991).

38. Cox, R.G., J. Fluid Mech. 338, 1 (1997).

39. Zemánek, P., Jonáš, A., Šrámek, L., & Liška, M., Opt. Commun. 151, 273 (1998).

40. Zemánek, P., Jonáš, A., Šrámek, L., & Liška, M., Opt. Lett. 24, 1448 (1999).

41. Ermak, D.L., & McCammon, J.A., J. Chem. Phys. 69, 1352 (1978).

BIOGRAPHICAL SKETCH

Aaron Robert Clapp was born in Minneapolis, MN, on February 3, 1974. He graduated from John F. Kennedy Senior High School in Bloomington, MN, in 1992. He then received a bachelor of chemical engineering degree from the University of Minnesota in 1996, and subsequently enrolled as a chemical engineering graduate student at the University of Florida. He joined the Dickinson Group in 1997 and began work with the Engineering Research Center for Particle Science and Technology. In 2000, he obtained a master's degree in biomedical engineering. He obtained his Ph.D. in chemical engineering in May, 2001.